LEVEL II

DAMAGE MECHANISMS AND FAILURE OF 3-D CARBON-CARBON COMPOSITES

P. H. Francis and C. T. Robinson

Southwest Research Institute

P. O. Drawer 28510

San Antonio, Texas 78284

Prepared for

OFFICE OF NAVAL RESEARCH

Department of the Navy

Arlington, Virginia 22217

NAVAL WEAPONS CENTER

China Lake, California 93555

February 28, 1979

SOUTHWEST RESEARCH INSTITUTE

SAN ANTONIO   CORPUS CHRISTI   HOUSTON

SECURITY CLASSIFICATION OF THIS PAGE (When Data Entered)

REPORT DOCUMENTATION PAGE		READ INSTRUCTIONS BEFORE COMPLETING FORM
1. REPORT NUMBER	2. GOVT ACCESSION NO.	3. RECIPIENT'S CATALOG NUMBER
4. TITLE (and Subtitle) DAMAGE MECHANISMS AND FAILURE OF 3-D CARBON-CARBON COMPOSITES		5. TYPE OF REPORT & PERIOD COVERED Interim Report, August 1977 — August 1978
		6. PERFORMING ORG. REPORT NUMBER SWRI-02-4982
7. AUTHOR(s) P. H. Francis D. T. Robinson		8. CONTRACT OR GRANT NUMBER(s) N00014-77-C-0510
9. PERFORMING ORGANIZATION NAME AND ADDRESS Southwest Research Institute P. O. Drawer 28510 San Antonio, Texas 78284		10. PROGRAM ELEMENT, PROJECT, TASK AREA & WORK UNIT NUMBERS
11. CONTROLLING OFFICE NAME AND ADDRESS Dept. of Navy, Office of Naval Research ATTN: Dr. A. M. Diness, Director Arlington, Virginia 22217		12. REPORT DATE February 1979
		13. NUMBER OF PAGES 87 + prelims
14. MONITORING AGENCY NAME & ADDRESS(if different from Controlling Office) Commander Naval Weapons Center ATTN: Mr. John Patton, Code 3161 China Lake, California 93555		15. SECURITY CLASS. (of this report) Unclassified
		15a. DECLASSIFICATION/DOWNGRADING SCHEDULE

16. DISTRIBUTION STATEMENT (of this Report)

Unlimited 93p.

DISTRIBUTION STATEMENT A
Approved for public release;
Distribution Unlimited

17. DISTRIBUTION STATEMENT (of the abstract entered in Block 20, if different from Report)

18. SUPPLEMENTARY NOTES

19. KEY WORDS (Continue on reverse side if necessary and identify by block number)

Composite Materials
Carbon-Carbon Composites
Thermo-mechanical Properties
Crack Initiation
SEM Fractography

20. ABSTRACT (Continue on reverse side if necessary and identify by block number)

Mechanical property characterization tests were conducted on specimens from a three-dimensional, cartesian orthogonally woven carbon-carbon (C-C) material. Tests consisted of tensile and rail shear, which were conducted at room temperature, and compression tests conducted at room temperature up to 2165°C (3930°F). Stress-strain characteristics and acoustic emission instrumentation were employed to infer the mechanics of the fracture initiation process. In addition, a specially developed axial loading stage integral to SwRI's ETEC scanning electron

DD FORM 1473 EDITION OF 1 NOV 65 IS OBSOLETE

328 200

SECURITY CLASSIFICATION OF THIS PAGE (When Data Entered)

20. ABSTRACT (Continued)

microscope facility was used to view and videotape the crack initiation and development processes. As a result of these studies, a tentative model is described to explain the mechanics of failure in 3-D C-C composites.

FOREWORD

The research reported herein was conducted by Southwest Research Institute under Contract N00014-77-C-0510 to the Office of Naval Research. The report summarizes work accomplished during the period August 1977 through August 1978. Dr. Arthur Diness was responsible for ONR program direction, and Mr. John Patton of the Naval Weapons Center at China Lake served as the Navy Project Engineer. The work was conducted under the supervision of Dr. Philip H. Francis, SwRI Project Manager, with Mr. Craig T. Robinson of SwRI carrying the responsibilities of Principal Investigator. Several other staff members contributed importantly to the research effort. Special acknowledgement is due to Dr. David L. Davidson, who conducted the fractographic studies in the SwRI SEM with axial loading stage facility, Mr. Henry Garcia for his work in running the room temperature mechanical characterization tests, and to Mr. Hans J. Muehlenhaupt for carrying out the high temperature tests.

iii

TABLE OF CONTENTS

LIST OF FIGURES

LIST OF FIGURES (Cont'd)

LIST OF FIGURES (Cont'd)

LIST OF TABLES

I. OBJECTIVES

Since the middle of this decade there has been ever increasing
potential for the use of advanced carbon-carbon (C-C) materials in se-
lected areas of defense hardware. These materials have good strength
retention at the high temperatures (~3000°C) found in, e.g., rocket
nozzle applications. Moreover, they generally have good erosion and
environmental tolerance when compared with other comparable materials,
such as pyrolytic graphite. However, the complex and unusual micro-
structural nature of three-dimensionally woven C-C materials demands a
more thorough understanding in order to predict thermo-mechanical per-
formance and reliability.

In 1977 the Office of Naval Research established a program of four
research projects to provide an integrated focus on problems of mechani-
cal characterization, fracture, processing, and microstructural analysis
of advanced C-C materials. Program management was coordinated through
the Naval Weapons Center at China Lake (Mr. John Patton).

It is within this program framework that the objectives of the
present project were defined. During the one-year effort reported here-
in, the main objective has been to gain new insight into mechanisms of
mechanical failure of a three-dimensional C-C material of cartesian
geometry. In order to meet this objective it was necessary to charac-
terize the strength and deformation properties of the chosen material in
various loading modes and at ambient and elevated temperatures. Acoustic
emission (AE) instrumentation was used in several of the tests in an
effort to evaluate the progression of damage by various microstructural
sources, e.g., interfacial separation, fiber breakage, and pullout, etc.
A series of tests was also conducted in a special loading stage developed
for the scanning electron microscope. These tests allowed the observa-
tion and videotaping of magnified regions of the specimen in real time
as damage developed under monotonic load.

The results of these tests have made possible initial insights
into how C-C materials begin to fail under different load states and
at various temperatures. As more work is accomplished toward this

project's objectives, it is believed that this newly-acquired knowledge
should lead to improved hardware design and reliability.

II. MATERIAL SYSTEM

The material system investigated in this project was a three-
dimensional, cartesian orthogonally woven carbon-carbon (C-C) material
supplied by Fiber Materials, Inc., Biddeford, Maine. FMI fabricated
two billets, Nos. 2695 and 2696, each being nominally 20.3 cm (8 in.)
long in the z direction and 10.15 cm (4 in.) in both the x and y direc-
tions. Half of billet No. 2696, i.e., a 10.15 cm (4 in.) cube of mater-
ial, was used in the present investigation; the remaining material was
distributed among the other three contractors* as prescribed by the NWC
Project Engineer.

The precursor for the fibers was HM-3000, a polyacrylonitrile
(PAN) yarn manufactured by Hercules, Inc., using a high-modulus process.
The matrix precursor was Ashland 240, a petroleum pitch. Each billet
was exposed to seven pitch impregnation and carbonization (PIC) cycles,
nine graphitization cycles, and three proprietary cycles. Densifica-
tion routing sheets for these billets are included in Appendix A.

The first PIC cycle is done in a vacuum at approximately 200°C.
This cycle gives the billet a good deal of its final rigidity. The
5000 psi PIC cycles are conducted at temperatures of 550 to 600°C. The
graphitization cycles are conducted at atmospheric pressure; the first
six are at 2600°C and the final three are at 2400°C. These temperatures
are the sighted (measured) temperatures. The actual billet temperatures
may be some 100° to 120°C higher.[1] The proprietary cycles at the end
of the fabrication process are very similar to the initial PIC cycle,
except that the billet is now impregnated with a resin rather than a
petroleum pitch. This type of cycle is typical of the final cycles in
the manufacture of propulsion materials.

Figure 1 shows the basic geometry of the material system. An
analysis of the geometry of a unit cell of this structure (Figure 2)
leads to the following relationships for the volume of the unit cell
V_c, volume of the yarn bundles V_y in the unit cell, and the fiber vol-
ume fraction V_f:

---

*Atlantic Research Corporation, UCLA, and the University of Wyoming.

3

$$V_c = (Y_x + Z_x)(X_y + Z_y)(X_z + Y_z) \tag{1}$$

$$V_y = X_y X_z (Y_x + Z_x) + Y_x Y_z (X_y + Z_y) + Z_x Z_y (X_z + Y_z) \tag{2}$$

$$V_f = V_y / V_c$$

$$= \frac{X_y X_z}{(X_y + Z_y)(X_z + Y_z)} + \frac{Y_x Y_z}{(Y_x + Z_x)(X_z + Y_z)} + \frac{Z_x Z_y}{(Y_x + Z_x)(X_y + Z_y)} \tag{3}$$

The matrix volume fraction, V_m, assuming the absence of voids, is simply $V_m = 1 - V_f$. The expression for V_f given above indicates that the <u>minimum</u> fiber volume fraction is 3/4 and occurs when the yarn bundles in all three directions have the same, square, cross-sectional dimensions. Any deviation from this condition will increase V_f; at the extreme, if the fibers in any one direction have vanishing cross-sectional dimensions, then $V_f = 1.0$--that is, the yarn bundles occupy the whole unit cell space. In the case of circular yarn bundles of equal diameter, the above expression leads to $V_f = 3\pi/16 = 58.9\%$.

In the case of the material system under study in this project, data supplied by Fiber Materials, Inc.,[2] from the preform geometry (see Figure 2) leads to the following dimensions: $X_y = X_z = Y_x = Y_z = 0.071$ cm (0.028 in.); $Z_x = Z_y = 0.086$ cm (0.034 in.). Based on these data the fiber volume fraction is, from Eq. (3), 75.23%. Another calculation of interest concerns the ratio of the area occupied by the fiber ends to the unit cell area on each of the three principal unit cell faces. These three ratios (one for each principal direction) are identical to the ratios of the fiber bundle volumes, in each of the principal directions, to the unit cell volume. For the present geometry these ratios in the x, y, z directions, respectively, are 0.2258, 0.2258, 0.3007, or in the proportions 30%, 30%, 40%. This means that the density of fiber ends in the z-direction is higher than in the other two principal directions by the ratio 4/3, indicating that (to a first-order approximation) the axial strength in the z-direction should exceed that in the x and y directions by 33%. Note that the areas of the yarn bundle ends are in the ratios 28.8%, 28.8%, 42.4%, and differ from the ratios given above because the unit cell is not a cube, but a parallelopiped.

It should be mentioned that these values differ from those of the supplier, which address the relative number of fiber ends on each side of the unit cell and consider not only spacing and number of ends per site, but also void geometry. The yarn volume fractions for both billets as computed by FMI are: 23.7%, 23.7%, 52.6%. The preform data sheet is included as Table 1.

TABLE 1. PREFORM DATA SHEET SUPPLIED BY
FIBER MATERIALS, INC.[2]

Property		Mfg. No. 2695	Mfg. No. 2696
Yarn Type		HM-3000	HM-3000
Yarn Ends/Site x,y		2	2
	z	5	5
Yarn Bundle Spacing x,y		0.056"	0.056"
	z	0.062"	0.062"
Preform Dimensions x		4.265"	4.290"
	y	4.288"	4.289"
	z	8.521"	8.571"
Weight (gms)		2073	2078
Preform Density (g/cc)		0.812	0.803
Fiber Volume		43.9%	44.4%
Yarn Volume Fractions x		23.7%	23.7%
	y	23.7%	23.7%
	z	52.6%	52.6%
Reinforcement Fractions x		10.9%	10.9%
	y	10.9%	10.9%
	z	24.1%	24.1%

The material system described above was chosen as a first step in gaining the experience necessary for studying the behavior of cylindrically woven materials. The geometry and processing of the material system used in this research were very similar to those currently employed in strategic rocket nozzles. By choosing a cartesian material system for initial characterization, smaller and simpler specimen geometries could be used, which in turn facilitated the assessment of the observed behavior.

III. PHYSICAL PROPERTIES

One of the concerns about the physical properties of the present billets, as well as of in-service billets, is whether or not there are substantial density gradients and, if so, what effect these gradients may have on the mechanical properties of the material. Table 2 shows tabulated results of four sets of density tests. Test samples were cubes, 1.3 cm (0.5 in.) on a side taken at points spaced equally from near the surface to the middle of the billet (see Figure 3 for exact locations within the billet).

The weights of the samples were determined both in and out of water, and the density calculated per ASTM D792 specifications:

$$\rho = \frac{0.9975}{1 + \frac{W_o - W_w}{W_a}} \tag{4}$$

where: W_o is the apparent weight of the wire hook partially immersed in the water, W_w is the apparent weight of the specimen, with wire hook, immersed in water, and W_a is the weight of the specimen (without wire hook) in air.

TABLE 2. MEASURED DENSITY GRADIENT DATA FOR
C-C BILLET (g/cc)

Measurement No. \ Specimen No.	1	2	3	4
1	1.9167	1.9238	1.8940	1.8982
2	1.8979	1.8782	1.8768	1.8709
3	1.9071	1.8743	1.8666	1.8691
4	1.8966	1.8725	1.8738	1.8689
$\bar{x}$	1.9046	1.8872	1.8778	1.8768
S.D.	0.0093	0.0245	0.0116	0.0143

6

Since the carbon-carbon material system is quite porous, it was anticipated that absorption of water during the tests might affect the density results. Thus, each of the samples was weighed four times, allowing three days between weighings to dry out. As seen from the data in Table 2, there was no consistent trend to absorb and retain water with successive weighings. Graphical results showing the density gradients are presented in Figure 4. There is a definite density gradient from the surface into the center of the billet; however, it should be noted that the total variation in density from the billet edge to the center was only 1.5%. The scale has been enlarged in the figure to show the gradient better. The standard deviation for each set of four measurements is also shown. It is likely that a density gradient of this size would not have an important effect on the mechanical properties of the material, although this statement would have to be verified by further testing. However, during the course of the tests on this project, there was no noticeable difference in mechanical properties between specimens taken from the billet surface and those from the center of the billet.

Another physical property which is of importance in applications of carbon-carbon material systems is the thermal expansion. Six specimens (three in the z-direction and three in the y-direction), 0.635 cm x 0.635 cm x 5.08 cm (0.25 in. x 0.25 in. x 2 in.), were sent to Fiber Materials, Inc., to be evaluated. Each specimen was measured with a quartz dilatometer in the temperature range from 20°C to 850°C (68°F to 1560°F). In each case, the data tracked a continuous curve; see Figure 5 for a typical example. As expected, the material showed a slight contraction, in each case reaching a minimum at approximately 350°C (660°F). Upon further heating, the material began to expand.

Measurements in the temperature range from 350°C to 2700°C were made with an optical (twin telemicroscope) dilatometer. A continuous plot was not possible, since measurements must be taken manually. Results for this part of the tests are typified by the results shown as Figure 6. The data for the optical dilatometer contain somewhat more scatter than those from the quartz tube dilatometer. The results from all of the tests are superimposed on a single master plot in Figure 7. The single fit

7

curve for each fiber direction is a visual fit through the curves at the lower temperatures and through the discrete points at the higher temperatures. Total expansion of the material at 2700°C was about 0.9% in the z-direction and 0.6% in the y-direction.

IV. MECHANICAL PROPERTIES

The purpose of the mechanical tests was two-fold: first, to produce a set of mechanical properties data for the material under simple loading conditions; and, second, to observe and analyze the failure modes of the material. The mechanical properties are discussed below, and a description of the failure processes is provided elsewhere.

The complete cutting scheme for the original billet, half of which was provided for the SwRI phase of the program, is shown in Figure 2. All specimen types were cut from the billet so that half would be tested along the z-direction (thicker fiber bundles) and the other half along the x- and/or the y-direction (smaller fiber bundles).

Mechanical tests were conducted on an MTS model 810, servo-hydraulic, closed-loop test system; see Figure 8. Since carbon-carbon materials tend to behave in a rather brittle manner, the tests were run under displacement control. Specimens were instrumented with acoustic emission pickups and a full array of strain gages. Strain gage and AE setups are described in more detail in a later section. Strain data were recorded on a Memodyne digital recorder with a 20-channel capability. Data were then taken from the digital tape through a Datel LPR-16 cassette recorder which introduced the data (in hexadecimal form) into a Hewlett-Packard 9830A mini-computer. Data were reduced and stored on a floppy disc for further use. Data could then be plotted on an HP 9862A calculator plotter interfaced with the mini-computer.

For the tension and compression results, it was found that the initial portion of the stress strain curves was sufficiently linear that a straight line could be fit to the points in this region. The slope of the resulting fit was taken as the elastic modulus of the material in the given fiber direction. In cases where a straight line fit to data is assumed, the coefficient of determination (R^2) for the fit is used as a measure of how closely the data track a linear relationship. An R^2 value of 1 (or 100%) indicates perfect compatibility of data points and linear fit; $R^2 = 0$ indicates that no linear relationship exists.

Table 3 presents a summary of the room temperature compression test results. The specimens were 1.27 cm x 1.27 cm x 2.54 cm (0.5 in. x

9

TABLE 3. SUMMARY OF ROOM TEMPERATURE COMPRESSION
TEST DATA

Specimen	σ_{max} (MPa)	$\bar{x}$ + S.D. (MPa)	Specimen Orientation	E (GPa)	% Fit	$\bar{x}$ + S.D. (GPa)
[1]C1	155			176	94	
C2	176	176 ± 18	z	---	--	163 ± 11
C2A	173			160	73	
C3	199			154	--	
C14A	101			66	--	
C15	101	103 ± 3	x	68	--	66 ± 2
C16	106			65	87	

[1] ℓ_o = 2 in.

0.5 in. x 1 in.), with the exception of No. C-1, which was 5.08 cm (2.0 in.) long. A comparison of the data for different compression tests shows that the elastic modulus for C-1 is slightly greater than that of the other specimens in the z-direction. It is also noted that the strength of C-1 is lower than that of the other specimens. The variations from the experimental mean of both the elastic modulus and ultimate strength are very close to the standard deviation of the sampling of test results. It is thus concluded that the longer test configuration had no significant effect on the test results.

The data for the compression specimens taken from the y-direction of the billet showed much less scatter. Results for both the elastic modulus and the ultimate strength in the three samples were very consistent.

In comparing the compression results in the two different directions, it is noted that the elastic modulus in the y-direction was approximately 40% of the modulus in the z-direction. The corresponding fiber volume ratio is 45%[*], and since the fibers are expected to be the primary load carrying components, this result is reasonable. Also, the

[*]See Table 1 and the related discussion in "Material System."

ultimate compressive strength in the y-direction was 40% of the strength in the z-direction.

It is pertinent here to mention that at present there is no satisfactory micromechanical constitutive theory for three-dimensional C-C materials. Such a theory, if available, would enable the prediction of the composite strength and stiffness properties from the constituent properties, although these constituent properties were not measured in the present investigation.

Another noteworthy result from the compression tests was that the transverse strains in all cases were very small. They were so low, in most cases, that they were below the resolution capabilities of the data acquisition equipment. Figure 9 shows all four transverse strain readings for specimen C-1 on an expanded strain scale. Figure 10 shows one of the transverse strains plotted on a scale with a longitudinal strain for comparison. Since this was a consistent result throughout the tests, it is concluded that Poisson's ratio for the material is practically zero.

One problem that was encountered in some of the early compression tests was specimen bending, as indicated in Figure 11. The two strain curves shown are from gages mounted on opposite sides of the specimen. This problem was solved by better alignment of the fixturing and closer tolerances in the degree of parallelism between ends of the specimens.

The tension specimens were 10.16 cm (4.0 in.) long with a cross section 2.54 cm (1.0 in.) wide by 0.635 cm (0.25 in.) thick, as shown in Figure 12. Beveled fiberglass tabs served to transfer the loads from the grips into the specimen. The resulting test section was 2.54 cm (1.0 in.) long. As in the compression specimens, one lateral and one longitudinal strain gage were placed on each face of the specimen within the test length.

Figure 13 shows typical curves for three of the longitudinal gages (the fourth gage shorted out) on a specimen oriented in the y-direction. The agreement among all of the gages is considered excellent. As for the compression samples, a straight line was fit to the initial portion of the stress-strain curve. The data fit the straight line very well in nearly every case. Again, as was found in the compression tests, the

11

transverse gages showed negligible Poisson contractions. Also shown, for comparison, in Figure 13 is one of the transverse stress-strain relations (Channel 14).

From a micromechanical description, an examination of the unit cell geometry shows that each yarn bundle is in physical contact with one other yarn bundle in each of the two orthogonal directions, as well as with two matrix pockets. A tensile loading will therefore introduce transverse tensile strains in the orthogonally-directed yarn bundles. If the yarn bundle can sustain the transverse strain without splitting or without separation at the interface between two yarn bundles in contact, there should be a global Poisson effect. There being no significant Poisson effect, however, it is concluded that splitting of transverse yarn bundles or interface separation may occur under tensile loading. The effect upon subsequent mechanical performance, if any, is unknown.

In reviewing the tensile results in Table 4, it can be seen that the direction of the thick fiber bundles (z-direction) has an effect on the mechanical properties even when the specimen is tested in a weaker direction. Specifically, the average tensile strength of specimens T-9, T-10, and T-11 is higher than that of specimens T-6, T-7, and T-8. Specimens T-9 through T-11 have the thick fiber bundles going through the thickness (i.e., normal to the specimen surfaces) and specimens T-6 through T-8 have the z-direction fibers oriented across the width of the specimens. The elastic moduli vary in a like manner to the strength properties in this instance.

The tensile specimens having the letter R in parentheses in Table 4 each had a reduced cross-section, as shown in Figure 14. This was done because in the original tests of specimens T-1, T-2 and T-3, the fibers were so strong that the specimens pulled out of the fiberglass tabs. In the subsequent tests of specimens T-2 and T-3, the specimens again sheared out of the tabs. It must therefore be assumed that the ultimate strengths for these specimens are not accurate, but that the calculations for the elastic modulus are representative, since the shear failures occurred in the nonlinear portions of the stress-strain curves.

Specimen T-12 also had a reduced section. Since it was presumed that the reduced sections in the z-direction specimens (T-1 to T-4)

TABLE 4.   SUMMARY OF ROOM TEMPERATURE TENSILE TEST DATA

Specimen	σ_{max} (MPa)	$\bar{x}$ ± S.D. (MPa)	Specimen Orientation	E (GPa)	% Fit	$\bar{x}$ ± S.D. (GPa)
[1]T1	126			138	98	
[1]T2(R)	153	[1]150 ± 26	z	140	82	154 ± 18
[1]T3(R)	138			174	97	
T4(R)	185			166	--	
TT1	331			174	100	
TT3	302	[2]297 ± 37	z	122	78	140 ± 29
[2]TT4	257			125	98	
T6	98			57	100	
T7	93	96 ± 3	[3]y	41	99	48 ± 8
T8	93			47	100	
T9	128			61	99	
T10	128	128 ± 13	[4]y	68	100	63 ± 10
T11	112			50	97	
T12(R)	145			72	97	

1 - slipped or sheared out of grips: σ(max) and $\bar{x}$ ± S.D. for data group may be inaccurate

2 - machine malfunction caused early failure: σ(max) and $\bar{x}$ ± S.D. for data group may be inaccurate

3 - x yarn bundles in thickness direction

4 - z yarn bundles in thickness direction

would affect the results, one of the y-direction specimens (T-12) also was tested with a reduced section to allow a comparison of the measured tensile strengths. The mechanical properties of T-12 can be compared to those of T-9, T-10, and T-11 (specimens with the same fiber orientation) to get an idea of the effect of the reduced section. The ultimate strength of T-12 was significantly higher (by two standard deviations) than that of the other three specimens, but the moduli were statistically equivalent for all four specimens. On the basis of this result, it is assumed that the tensile strength values for T-2, T-3, and T-4 will be 15% to 20% high, and that the values for elastic modulus should be reasonably accurate.

13

In an effort to develop a tensile fiber failure in the z-direction, specimens TT-1 through TT-4 were machined to have a thickness of approximately 0.318 cm (0.125 in.), or two unit cells, and a width of about 1.27 cm (0.5 in.). As can be seen in Table 4, the tensile strengths of the thin specimens are almost double those of the thicker samples. However, the difference in elastic moduli is less than one standard deviation, leading to the tentative conclusion that there is no significant change in modulus with changes in specimen size. It is concluded from the above results, however, that the strength of this material is dependent on specimen dimension. More insight into effects of scale will be gained during subsequent investigations.

Rail shear tests were conducted to produce shear loading along a plane parallel to the loading direction (Figure 15). Strain gages for the shear specimens were aligned parallel to the loading axis, perpendicular to the loading axis, and at 45°. Figure 16 shows a typical plot of all six strain readings. Channels 2 and 8 (noted on curves) are at 90° to the loading axis, channels 4 and 10 are parallel to the load axis, and channels 6 and 12 are at 45°. As can be seen, the deformation is highly nonlinear, and it is not possible to fit a straight line to any portion of these stress-strain curves. Thus, the only results tabulated are for the ultimate strength; these are given in Table 5. It is interesting to note that shear planes perpendicular to both the y- and the z-fiber directions failed at approximately the same stress levels. Apparently, the fiber strength has little effect on the shear strength of this material.

The most remarkable phenomenon in the shear tests was the amount of deformation the material could sustain before fracturing. Figure 17 shows a loading sequence of specimen S-2, beginning at zero load and progressing to a maximum shear stress of approximately 2500 psi. At this point the inelastic deformation continued, but the load-carrying ability of the material began to decrease. As shown in Figure 18 the residual deformation in the specimen is substantial.

The final mechanical test sequence consisted of high temperature compression tests which were to be run at 1370°C (2500°F) and at 2760°C (5000°F) inside a Centorr Model M60-3X8W-WM-2-25 environmental chamber. However, test conditions necessitated use of a larger set of heating

14

TABLE 5. SUMMARY OF ROOM TEMPERATURE RAIL SHEAR
TEST DATA

Specimen	max (MPa)	$\bar{x}$ + S.D. (MPa)	Specimen Orientation
S1	14		
S2	17	15 ± 2	z
S3	14		
S4	--		
S5	--		
S6	11	14 ± 4	1_y
S7	17		
S8	--		

1 - z yarn bundles in thickness direction

elements than had previously been used at SwRI, and the maximum tempera-
ture attainable with the large heating element was 2200°C (4000°F).
Even at this temperature, hot spots in the furnace caused warping of
some portions of the heat shields. Therefore, the high temperature
tests were conducted at 1370°C (2500°F) and at 1930°C (3500°F).

Table 6 shows a tabulation of the high-temperature compression
results. Also listed, for comparison with the room temperature com-
pression data in Table 2, are the mean values. It should be noted that,
in general, the strength increases with temperature. This result is
seen for both fiber directions. However, the stiffness of the material
appears to decrease with increasing temperature. The calculation of
the elastic modulus at high temperature involved a correction to account
for the compliance of the machine and the fixturing. When a test was
run, the compliance of the machine and the fixturing, which was measured
separately, was subtracted from the apparent specimen compliance, re-
sulting in the compliance for the specimen only. From this compliance
value, the stiffness was calculated. Although sound in theory, this
method admits room for experimental error.

TABLE 6. SUMMARY OF HIGH TEMPERATURE COMPRESSION TEST DATA

Specimen	Specimen Orientation	Temperature (°F)	σ_{max} (MPa)	Mean σ_{max} (MPa)	E (GPa)	Mean E (GPa)
C-6	z	2500	157	162	15	16
C-7	z	2500	168		18	
C-19	y	2500	118	120	7	8
C-20	y	2490	122		9	
C-11	z	3540	198	204	13	13
C-12	z	3530	209		13	
C-21	y	3520	160	152	9	8
C-22	y	3930	---		6	
C-23	y	3550	143		10	

16

V. DAMAGE MODES

Damage mechanisms were observed using three different procedures: acoustic emission monitoring during the mechanical tests gave valuable insights into the initiation of failure mechanisms; post-test failure analysis gave a more direct indication of failure modes; and observation of specimens under load in a scanning electron microscope (SEM) allowed real-time observation of initiation of progression of damage leading to failure. These three methods of observation will be discussed in turn.

Acoustic Emission

Acoustic emission (AE) signals were monitored with a 0.635 cm diameter by 0.238 cm thick (0.25 in. diameter x 0.0938 in. thick) PZT-5 crystal, mechanically pressure-coupled to the specimen surface. The transducer was found to have a resonant frequency of about 200 KHz. Data for the compression tests and for many of the tension tests were displayed in bar graph format by the system recorder. As a preliminary indication of the appearance of the signals, a 0.5 mm lead from a lead pencil was broken on the surface of one of the specimens; Figure 19a shows the resulting RF signal and Figure 19b is the accompanying bar chart. The horizontal axis represents the magnitude of the signals, and the vertical axis is a log scale which represents the number of re-corded signals at each magnitude. Note that there are a number of low amplitude "background" counts at four of the lower amplitudes and a reading at a single, distinct, higher amplitude. It was discovered during the actual testing that the signals of higher amplitude also had a longer duration.

Figure 20 shows three of the bar charts during the test of speci-men C-10. This is a typical sequence of AE data taken from a compres-sion test. Figure 20a is a display of the cumulative counts immediately following the first audible noise. As can be seen, there is some small amplitude noise and a number of counts at an isolated high level. As the test progressed, the number of lower amplitude signals increased substantially. The high-level signals also became more numerous, and signals from many of the higher ranges appeared. Figure 20b shows a

17

cumulative count of maximum load for this test. This pattern of numerous low-level counts, decreasing with increasing amplitude (with a small increase in quantity of the highest amplitude ranges), was found to be typical of all of the tests. Figure 20c shows the cumulative display at the end of the compression test. This is not a true indication of the AE pattern after a test, for reasons discussed below; but it does give some indication as to the significance of the signals of different amplitudes. Figure 20b is considered an accurate indication of the AE pattern developed during a test, since it is the pattern immediately following the peak load on the specimen.

Figure 21 shows a typical load vs longitudinal displacement plot for a compression test. There was a major drop in stress at, or perhaps just below, the maximum stress a specimen could sustain. This drop in stress was usually accompanied by a corresponding drop in strain, since the onset of damage usually occurred at the ends of the specimen where the load was applied. This drop coincided with the first large audible cracking noise and resulted in a cumulative AE count as shown in Figure 20a. Following this unloading phenomenon, the specimens again began to accept increasing loads. During this reloading period, significant additional low-level AE signals and a substantial number of intermediate-level signals were recorded. It was, in general, a very quiet period for acoustic noise in that little or no high-level AE signals were recorded. The stress level reached just prior to the first breakdown was usually just below the maximum stress attained in any given test. Upon the first reloading, the peak stress was attained and was immediately followed by a second loud audible crack. Once again, the audible crack coincided with a significant number of high-level acoustic signals (Figure 20b). In most cases the subsequent cycles of reloading did not reach peak stress, but declined steadily. At this point the specimen was considered to have failed. The subsequent cycles emitted much softer audible noise, and during these reloadings many more counts were recorded in the intermediate levels of the AE plot. By the end of the test the cumulative plot of all AE signals looked similar to Figure 20c.

In the period following the second load decrease, it was noticed that the specimens began to spall (brooming phenomenon) at the top or

18

the bottom surface of the specimen. The specimens would then continue
to break down through this mechanism until the test was terminated. It
was concluded that this process resulted in the intermediate-level AE
signals because the longer a compression test ran, the more intermediate
counts would be recorded. This phenomenon probably had no effect on the
measured mechanical properties since it occurred very late in the test
sequence.

The same acoustic emission monitoring process was used for most
of the tension tests, and the results were very similar, as seen in
Figure 22. Figure 22a shows the cumulative AE count at 134 MPa (19.4
ksi) stress. This was very early in the test, and the only signals were
low-level noise. Figure 22b shows the cumulative AE spectrum after the
first loud audible crack was heard. It is presumed that the counts at
the single high amplitude were from fiber breakage. Finally, Figure
22c shows the AE accumulation at the end of the test. At the end of
the tension test the low-level noise had filled in somewhat, and high-
level signals had been recorded at several different amplitude ranges.
In contrast to the AE accumulation at the end of the compression tests,
low- and medium-amplitude signals were much less numerous in tension.
This was probably due to the fact that the compression test had no defi-
nite failure point, and as the tests continued, the specimens began to
crumble and spall at the ends.

A second method of logging the AE data was used for several ten-
sion tests and for two of the shear tests. Figure 23 shows the results
for Specimen TT-3. Beginning with the bottom channel, the first channel
is load: full scale is 5000 lb, which corresponds to an applied stress
of 539 MPa (78 ksi). The second channel is a simple count rate of all
counts above a 10 mV threshold, with a full scale of 5V. The third is
a blank channel. The fourth, fifth, and top channels are accumulated
ring-down counts with respective thresholds of 400 mV, 100 mV, and 10
mV. Full scale for these three channels is 65,536 counts.

It can be seen that the first significant acoustic noise occurred
when the load curve showed the first drop. The count rate registered
a substantial amount, and the accumulated ring-down counts for 10 mV
and 100 mV thresholds increased noticeably. The acoustic noise then
abated until the load curve approached the point at which it began to

19

level out. At this time the acoustic emission again increased, and substantial increases were recorded in all three ring-down accumulations. The increases continued until catastrophic failure of the specimen.

Similar data for a shear test are shown in Figure 24. As the load increases, the AE activity increases up to a point, then it appears to remain constant. Increased AE activity is observed just before peak load and again just as the load begins to decrease. The activity as load begins to decrease appears to be the most significant of the entire test. Later in the time sequence there is a more rapid decrease in load carrying ability of the specimen. This event is marked, not by increased noise during (or just prior to) the load drop, but by a temporary lull in the AE activity following the drop. This is presumably due to the stress redistribution within the material, before the load again begins to increase. There is a final burst of activity at the end of the test, but it is thought that this was due to the specimen shearing out of the rail fixtures. Evidence of this is seen in Figure 25, which shows a pinned hole which sheared out at the end of the test.

Due to the constant, moderate intensity, AE activity during the shear tests and the extreme amount of deformation during these tests, it is presumed that an accumulated count of signals within given amplitude ranges (as described for compression and earlier tension tests) during the shear tests would show a great deal of low- and intermediate-level signals and very few high-amplitude signals.

Based on the above observations, it was concluded: (1) that the AE signals of lower amplitude could be attributed to failure (crumbling or shearing) of the matrix material; (2) that the intermediate-amplitude signals were due in part to fiber crippling during stress redistribution, but perhaps more significantly to the "brooming" (spalling) failure encountered in the later stages of the compression tests; and (3) that the high-level signals were associated with sudden fiber failure. The consistency of these results lends a great deal of credibility to acoustic emission as a method of monitoring the mechanical integrity of carbon-carbon composites under applied loads.

20

Post-Test Failure Analysis

In analyzing the specimens after they had failed, it was noticed that the orientation of the strong fiber direction had significant influence on the mode of failure. Figure 26 shows the failure surface of specimen T-6. The thick fiber bundles are oriented across the width in this case, and the fiber bundles broke off straight across the specimen. There was very little, if any, apparent shear between the fibers and matrix regions. In contrast, specimen T-4 (Figure 27), in which the strong fiber direction is along the loading axis, showed a much greater tendency for the fibers to shear out of the matrix rather than fail in a tensile mode. There is presumably a great deal of shear deformation since the fiber bundles failed at different locations. If there were no shear deformation, the fiber bundles would all tend to fail along the same plane since a local failure of one bundle would cause a stress concentration and redistribution in the same region. However, the seemingly random locations of fiber bundle breakage indicates that substantial shear deformation may have distributed the stress concentrations along the test length. A direct indication of the shear during the tensile tests can be seen in the end of specimen T-4 (Figure 28). It is obvious that the longitudinal fiber bundles have pulled away from the transverse fiber bundles, even though all of the fibers failed within the test length of the specimen (refer back to Figure 27). Further examples of the shear deformations were seen in the tests of the thin tensile specimens (Figure 29). In many of these tests, in which the specimens were only two unit cells thick, some of the fiber bundles pulled completely out of the supporting structure without breaking.

Several interesting phenomena were observed during post-test examinations of the compression samples. The most obvious damage was a "brooming" effect (Figure 30). As mentioned earlier, this effect became obvious after the specimen had ceased to carry peak load. It is not believed that this damage mechanism had any effect on the ultimate strength, but once the specimen began to crumble in this manner, it continued doing so at a lower load than was required to initiate the process. This brooming phenomenon was found in specimens oriented in both the y- and z-directions.

Another characteristic that was noticed in many of the failed compression specimens was that some of the weak (i.e., x or y) fiber bundles on the free surface oriented perpendicular to the loading direction tended to be squeezed out of position, almost to the stage of being sloughed off (Figure 31). The specific time at which this event occurred was not noted. Thus, it is not known if it was due to Poisson strains or was a result of the buckling or crippling of interior fiber bundles. It is possible that one or more longitudinal fiber bundles at a location just under the surface could buckle and outwardly push a lateral bundle which was originally at or near the surface, thus giving the observed result. This deformation of lateral fiber bundles was observed in tests at all temperatures, and in both the y- and z-orientations. Like the brooming-type damage, this lateral displacement mode was noticed only in the later stages of strain: i.e., after the specimen had ceased to support the peak load and had begun visibly to fail.

There was one failure mechanism that was noticed only in some of the high-temperature compression tests. Specimen C-20, oriented in the y-direction and tested at 1370°C (2500°F), showed an oblique fracture surface (Figure 32) much like a conventional shearing-mode failure. Specimens C-11 (Figure 33) and C-12, oriented in the z-direction and tested at 1927°C (3500°F), also failed through a shearing mode. The test of specimen C-11 was stopped before complete failure. The angle of the failure surface, in all three cases, was approximately 25° to 30° from a plane normal to the loading direction.

Characterization of the stress-strain curves for the compression tests indicates that most of the specimens failed gradually with increasing load. However, specimens C-11 and C-12 failed suddenly and catastrophically as shown in Figure 34. Even through C-20 had an oblique failure surface, it did not fail catastrophically as did C-11 and C-12. It appears that the higher temperatures have a tendency to render the matrix material somewhat stronger and more brittle. This would explain the shear-mode failure surfaces and the more sudden failures as well as the slightly higher compressive strengths at the high temperatures.

The shear specimens, in most cases, sheared out of the pinned grips (Figure 35) before they failed along the intended slip plane. As mentioned in the previous section, there was substantial elastic

and plastic deformation in these specimens. Figure 36 shows a shear specimen after a test. The amount of permanent deformation is readily visible. The only specimen which did not behave in this manner was S-1, which failed suddenly and in a brittle fashion (Figure 37). The reason for this seemingly erratic behavior is not known. It should also be noted that the compressive strength of S-1 was right at the mean value for the five valid shear tests. Thus, whatever the cause of the brittle behavior, it did not seem to affect the strength of the material.

Observations in the SEM

Observation of specimens, under load, in a scanning electron micro-scope (SEM) proved to be a most valuable method of describing damage modes from initiation to final failure. SwRI's ETEC Autoscan SEM has been fitted with a load stage capable of applying tensile loads up to 4450 newtons (1000 lb) force. The details and capabilities of this specially designed load stage are given in Appendix B. Figure 38 shows the loading stage with one of the carbon-carbon specimens.

The load-carrying mechanism for this loading facility consists of two pins at the edges of each end of the specimen (Figure 39), and a specimen must have a suitable shear strength to distribute the load across the specimen and through the test section. Previous tests had shown that the carbon-carbon material did not itself have a sufficient shear strength; therefore, aluminum tabs were bonded to the specimens to facilitate the shear transfer.

All of the SEM specimens were machined with a reduced cross-section as shown in Figure 39. This was done to localize the damage initiation so that it could be observed in the limited area covered by the electron beam at any given instant. Also, some of the specimens were notched to localize damage initiation even more.

Upon observing several of these specimens it became apparent that damage initiated in a shear mode in many cases. Figure 40 shows a crack which initiated due to slip between a yarn bundle and a matrix region. It should be noted that the fibers were oriented at an oblique angle to the specimen surface due to the shape of the test section (constant ra-dius reduction), and this configuration would obviously have had an in-fluence on the initiation mechanism. Figure 41 shows a similar crack

23

running across the top edge and down the front face of specimen SEM-14. The overall crack configuration indicates that the initiation occurred in a sliding mode. (The loading is outward in a horizontal direction for all figures unless noted otherwise.) Once again the initiation was apparently due to the slip between a yarn bundle and a matrix pocket, yet the crack actually developed in the matrix region adjacent to the yarn bundles rather than at the fiber-matrix interface.

Another specimen configuration which showed an apparent shear-mode initiation was a notched specimen. Figure 42 presents a matched stereo pair of a damaged region under a notch. Under a stereo viewer, the effect of the horizontal (x-direction) displacement difference between a loaded and unloaded specimen can be seen as a topographic (z-direction) effect. This phenomenon is described in Reference 3. It is apparent that the damage initiated in a shear mode between the fiber and matrix regions proceeding in both directions from the notch root. The crack to the left abruptly changed to an opening mode crack (turned almost straight down), while the crack on the right proceeded along the interface region for some distance before slowly turning perpendicular to the loading direction (downward).

The crack network in Figure 42 gives a fairly good indication of the general pattern of crack growth in this three-dimensional material. The cracks, on either side of the notch, originated in a shear mode in the proximity of a fiber-matrix inerface, and then changed, with varying speeds, to opening mode cracks. The crack on the left changed very abruptly to a direction perpendicular to the applied load, and the crack on the right curved very slowly, never actually reaching a point where it had changed directions by a full 90°.

Both cracks, as they progressed through the matrix region, favored running through the larger voids present, even when the voids were somewhat out of the path of the crack. As the propagating cracks approached other longitudinal yarn bundles (lower regions of Figure 42), they again changed directions and proceeded along the interface region, parallel to the longitudinal bundles. As the cracks continued to propagate along the longitudinal yarn bundles, they encountered no apparent difficulty in shearing through the transverse yarn bundles. That is, cracks propagating in a shear mode near the fiber bundle/matrix interface favored

24

shearing through transverse bundles as they were encountered, rather than arresting or redirecting themselves in the mode 1 direction. This result is further evidence that the yarn bundles, as well as the matrix material, are very weak in shear.

A typical crack pattern for a single crack is found in Figure 40. Initiation was at a shoulder where the yarn bundle and matrix region developed considerable shear stress (top of photo). The crack then turned rather abruptly from shear mode to opening mode (horizontal to vertical orientation) and propagated through the matrix region until it approached a longitudinal yarn bundle. At this time it turned back to a direction parallel to the yarn bundle (shearing mode) and propagated along this direction until the specimen failed.

Failure of the SEM specimens appears to have developed by the same mechanisms as failure of the tensile specimens. In many areas of the specimen, yarn bundles would shear out of the matrix so that the fiber failure would not be at the same location as the matrix failure. Note in Figure 43 that the matrix regions have failed directly beneath the notch, but the two lower yarn bundles (the upper bundle was cut when the specimen was notched) apparently failed at another location. In specimen SEM-21 (Figure 44), which was also notched, the yarn bundles all failed directly below the notch, but the matrix failure occurred as far as one-quarter inch away from the fiber failure. In specimen SEM-24, the matrix failure was all directly below the notch and much (but not all) of the fiber failure was in the same vicinity.

In some of the specimens which failed completely, the yarn bundles pulled completely out of the specimen without fracturing. This failure mechanism was not limited to any one particular orientation. Figure 45 shows a z-direction specimen in which the fibers pulled out of the matrix, and Figure 46 shows a y-direction specimen in which most of the longitudinal yarn bundles remained unbroken.

The conclusion from the above discussion is that the fiber breakage, when it does occur, is of a rather random nature reflecting the highly redundant structure of the material system. The location of fiber fracture seems to depend on weaknesses in individual bundles rather than any stress concentration due to notches or other physical characteristics. In this respect, this material could be considered to

25

be insensitive to notches. However, the notches do help facilitate differential shear strains which lead to the initiation of the damage mechanisms. The other characteristic which facilitates high shear stress (and therefore strains) is the compliance of the matrix material compared to the fibers. The yarn bundles seem to be much stiffer (in the fiber direction) than the matrix pockets.

It was mentioned earlier that as shear cracks propagate along longitudinal yarn bundles, a crack develops in the matrix material in the immediate vicinity of the matrix-fiber interface. The same phenomenon was noticed between the transverse bundles and matrix regions as cracks developed in an opening mode (vertical cracks in Figures 43 and 44). The more nearly square regions on the faces of these specimens are the ends of z-direction fiber bundles. The thinner rectangular regions, with larger apparent voids, are matrix pockets. It was thought that the cohesion between fibers in a bundle would not be very strong. However, when opening cracks developed, they developed in the matrix regions immediately adjacent to and parallel to the fiber bundles. Thus the fibers appear to have a bond between them that is stronger than the matrix material.

VI. CONCLUSIONS

Efforts were made during this project to describe failure initia-
tion processes in a three-dimensional Cartesian orthogonally woven C-C
material. The billet used in this investigation, supplied by Fiber
Materials, Inc., of Biddeford, Maine, used HM-3000 fibers, had a density
of 1.89 and was constructed with yarn volume fractions of 23.7%, 23.7%,
52.6%. The conclusions presented below are based on measurements and
observations regarding physical and mechanical behavior, as well as
damage initiation, made during this exploratory effort.

1. Density gradients appear small: a decrease of 1.5% in density
    was measured from the surface to the center of the 10.15 cm
    (4 in.) billet cube.

2. The thermal expansion is a minimum (and slightly negative) at
    about 350°C. At higher temperatures it increases, with the z-
    direction expansion some 50% greater than that in the trans-
    verse directions; e.g., at 2700°C $\alpha_x = \alpha_y = 2.2 \times 10^{-6}$/°C and
    $\alpha_z = 3.3 \times 10^{-6}$/°C.

3. Results from room-temperature tension and compression tests
    indicate that the Poisson ratios are virtually zero.

4. Compression strength increases with temperature: e.g., speci-
    mens of both y and z orientations showed a 26% strength increase
    from 1370°C to 1930°C (2500°F to 3500°F). The compression modu-
    lus, however, decreases markedly with increased temperature.
    At high temperatures the matrix material appears to have more
    strength and to become more brittle than at room temperatures.

5. Tensile strength varies with test direction approximately in
    proportion to the ratio of yarn bundle volume. At room tempera-
    ture the tensile stiffness and strength properties are comparable
    to the compression properties.

6. The material is rather weak and highly ductile in shear; shear
    strength is not strongly related to slip plane orientation in
    the principal directions.

7. There may be a scale effect in strength due to specimen size
    (the smaller the specimen the greater the strength), but no
    scale effect was found in modulus.

8. Acoustic emission can be used effectively to distinguish dam-
    age sources: low amplitude is identified with matrix crumbling
    and with shear failures; intermediate amplitude signals are

indicative of fiber crippling and of spalling at the ends of
compression specimens; high amplitude signals result from
complete, sudden failure of fibers.

9. Cracks appear to originate in matrix pockets, near yarn bundle/
    matrix pocket interfaces, in a shear mode. The mechanism for
    this is possibly the stiffness difference between the matrix
    and the yarn bundle (in the fiber direction), which leads to
    shear strains in the matrix. Cracks propagate generally in an
    opening mode configuration, running through large matrix voids,
    then redirecting along transverse yarn bundle interfaces while
    shearing easily through bundles in perpendicular directions,
    then jumping back again to the opening mode configuration.

10. Yarn bundle breaks are rather randomly distributed over a
    material volume, indicative both of the high nonhomogeneity
    within the microstructure and of the redundant nature of the
    material system. Global fracture of the material appears to
    be a result of the coalescence of numerous small cracks, which
    link together to form a critical macrocrack.

REFERENCES

(1)   Per telecon between Jon Wilson of FMI and Craig Robinson of
        SwRI, July 10, 1978.

(2)   Letter from Jon Wilson of FMI to P. H. Francis of SwRI dated
        September 19, 1977.

(3)   Davidson, D. L., "Fatigue Crack Tip Displacement Observation,"
        Journal of Materials Science, Vol. 14, p. 231, 1979.

FIGURES
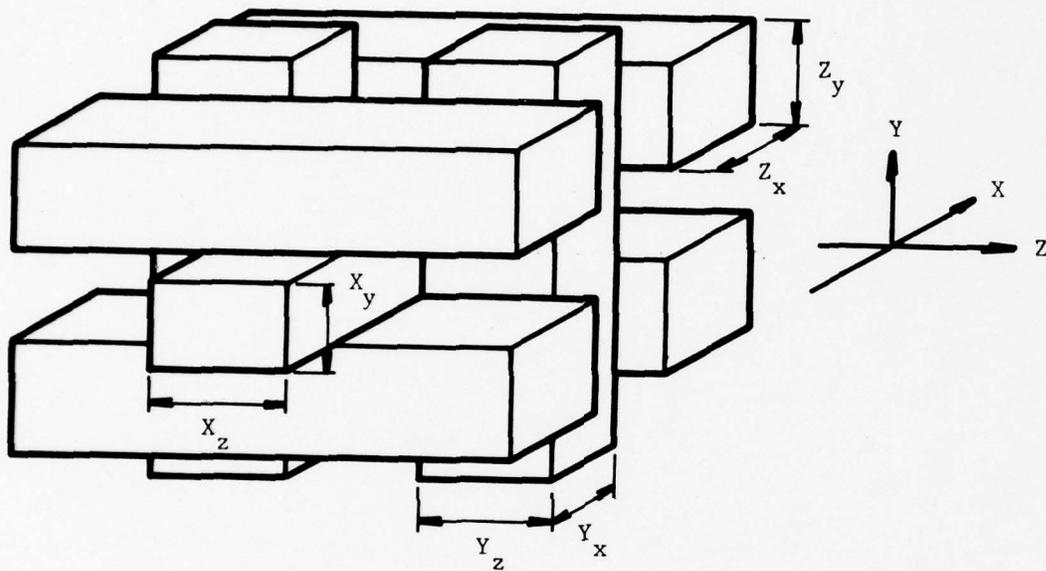
FIGURE 1.   BASIC GEOMETRY OF 3-D CARBON-CARBON MATERIAL
            SYSTEM WITH RECTANGULAR YARN BUNDLES.

32

.062"

0.62"

.056"

Z DIRECTION
5 ENDS/SITE
OF HM-3000
(15,000 FILAMENTS)

X DIRECTION
2 ENDS/SITE
OF HM-3000
(6000 FILAMENTS)

Y DIRECTION
2 ENDS/SITE
OF HM-3000
(6000 FILAMENTS)
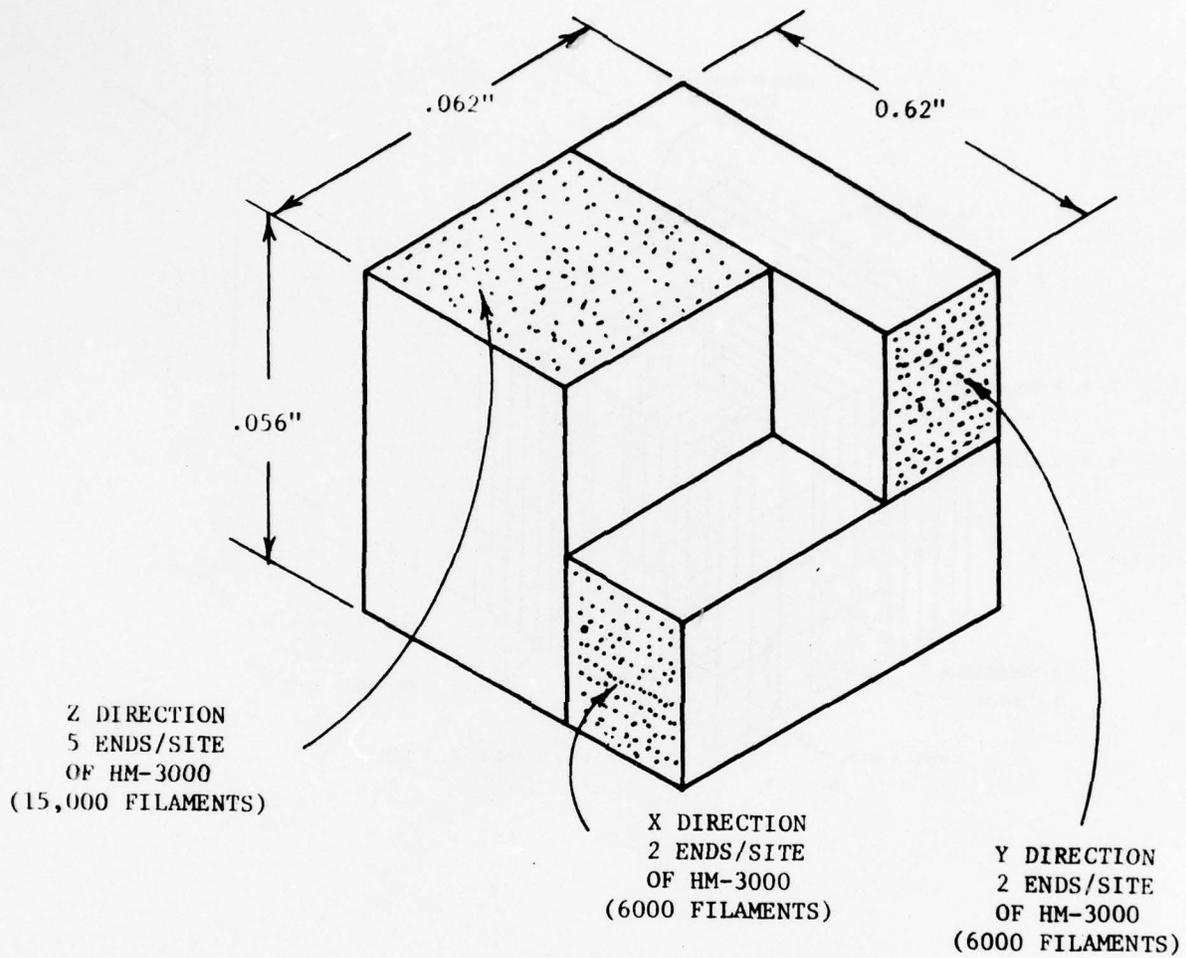
FIGURE 2. SCHEMATIC DRAWING OF UNIT CELL STRUCTURE FOR 2,2,3
CARBON-CARBON MATERIAL. DIMENSIONS FURNISHED BY
SUPPLIER (FIBER MATERIAL, INC.).

33
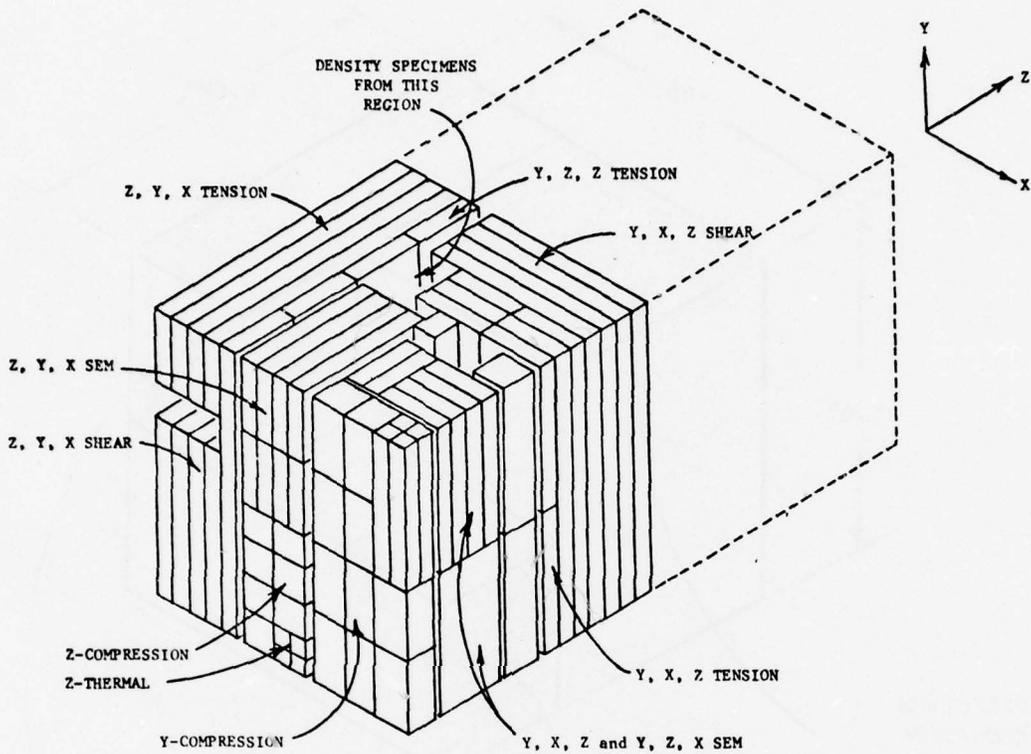
FIGURE 3.   CUTTING SCHEME, FOR BILLET NO. 2696, WHICH PRODUCED MECHANICAL
TEST SPECIMENS AS WELL AS DENSITY AND THERMAL EXPANSION SPECI-
MENS.
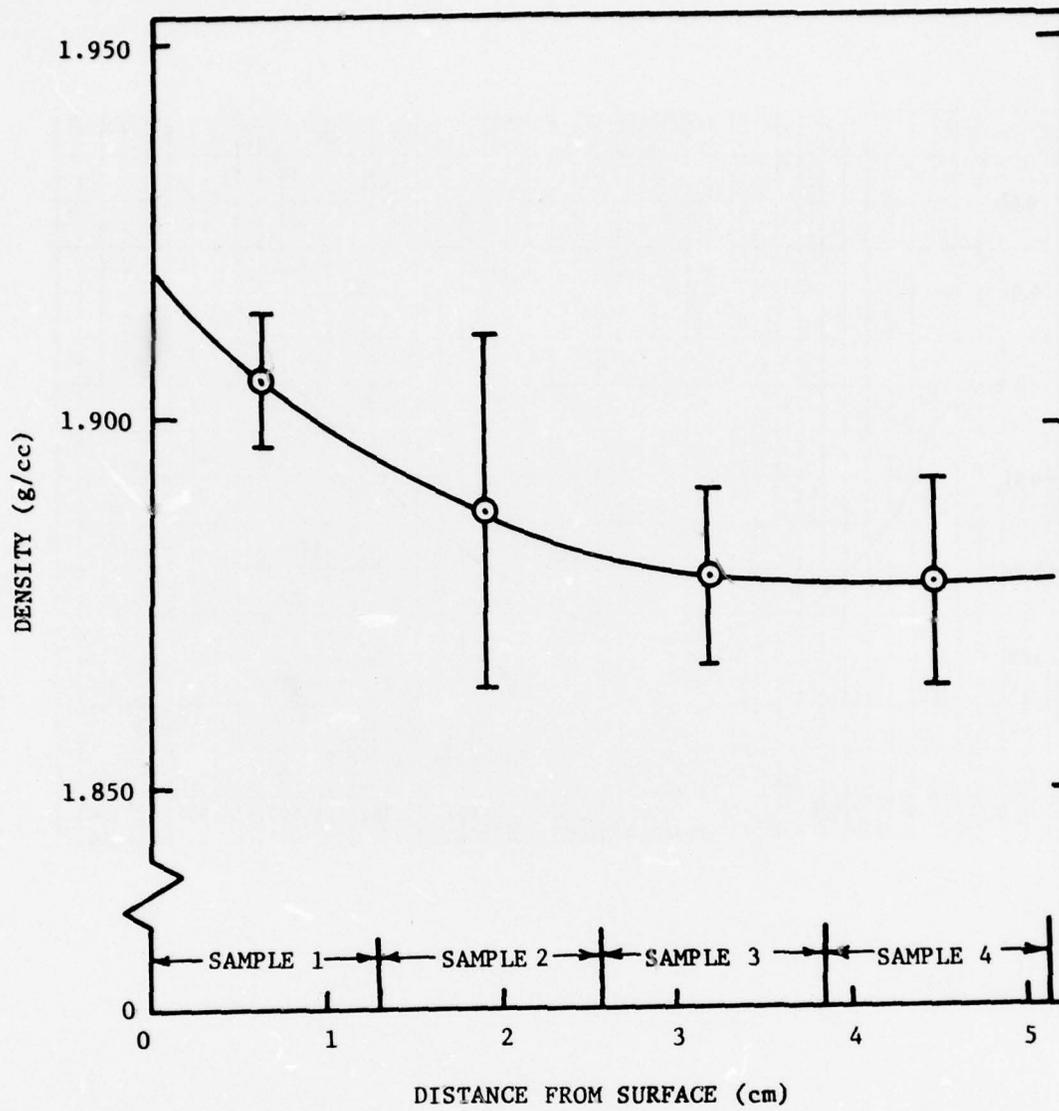
FIGURE 4. DENSITY PROFILE OF AS-RECEIVED CARBON-CARBON BILLET.
DENSITY SPECIMENS RANGED FROM AN OUTSIDE SURFACE TO
THE CENTER OF THE BILLET.
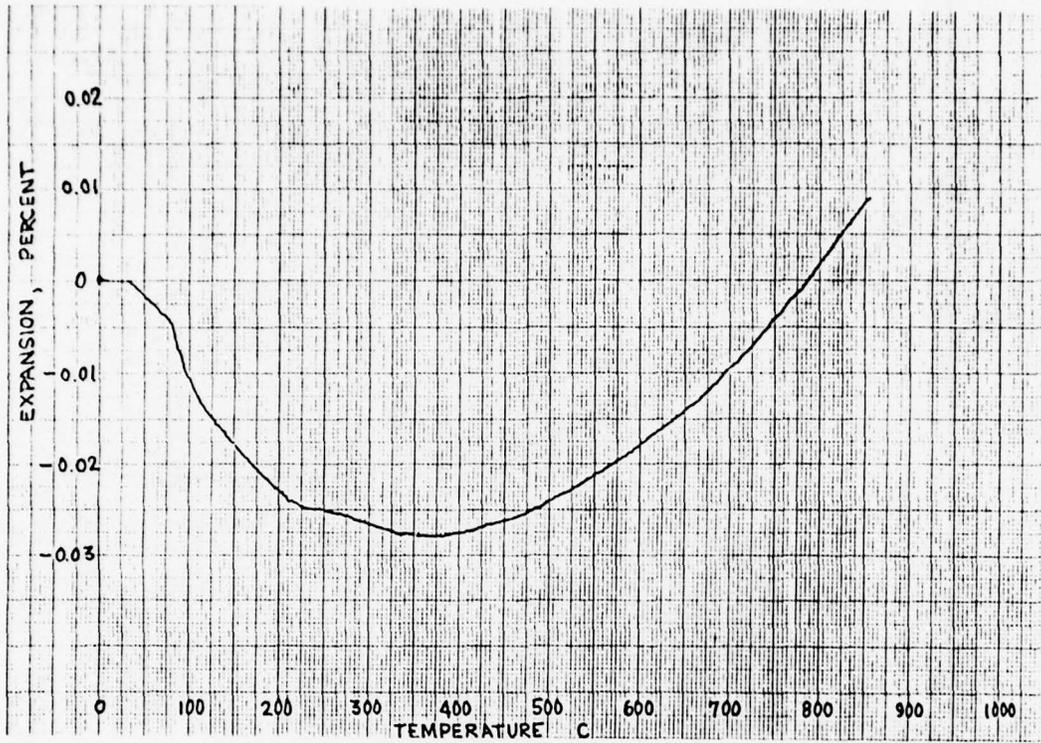
FIGURE 5. TYPICAL THERMAL EXPANSION CURVE FOR THE LOWER TEMPERATURE
RANGES AS RECORDED BY A QUARTZ-TUBE DILATOMETER. SPECIMEN
NO. TH-1.

36
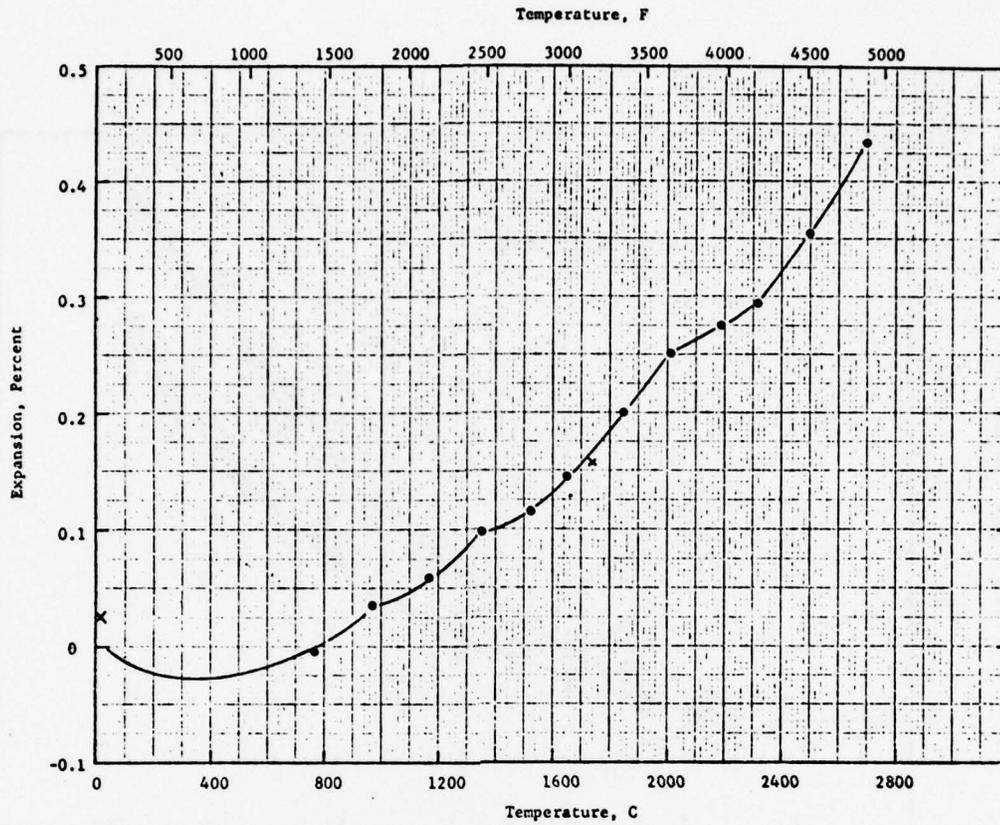
FIGURE 6. TYPICAL THERMAL EXPANSION PROFILE FOR HIGHER TEMPERATURE
RANGES AS OBSERVED IN AN OPTICAL DILATOMETER. SPECIMEN
TH-1.
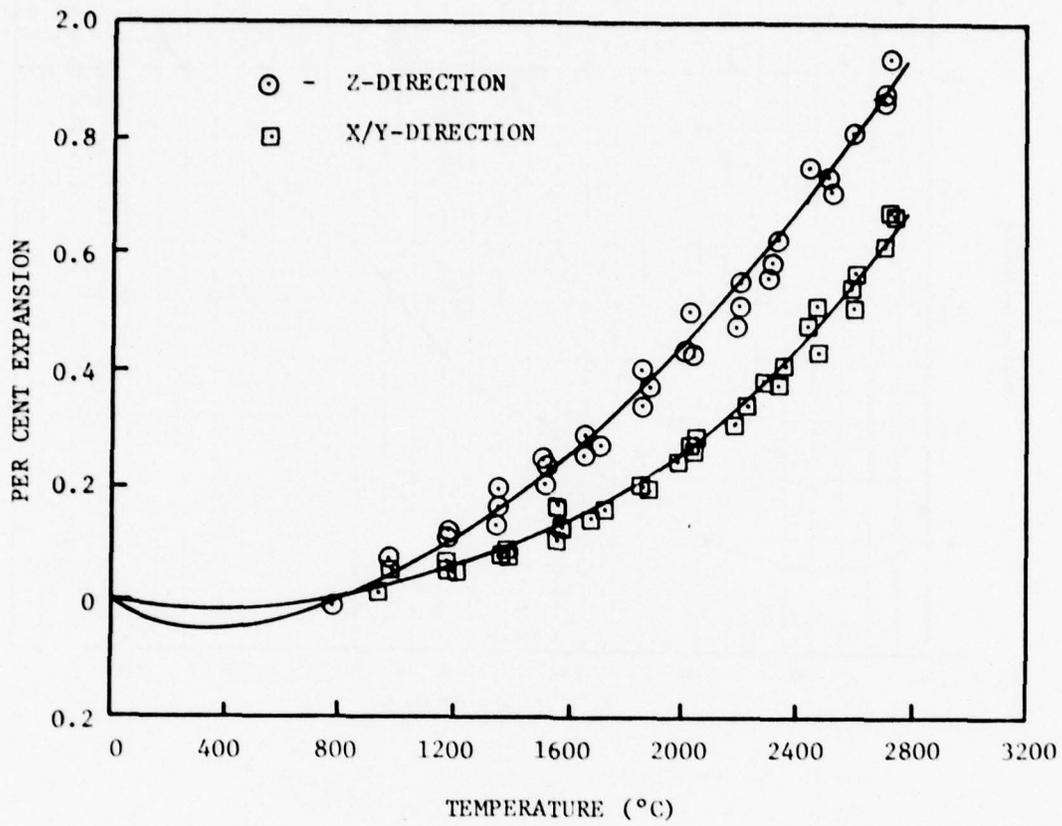
FIGURE 7. COMPLETE THERMAL EXPANSION CURVES FOR BOTH THE
Z- AND THE Y-DIRECTIONS, FROM 20°C TO 2700°C.
THE CURVE SHOWN IS A VISUAL FIT.

38
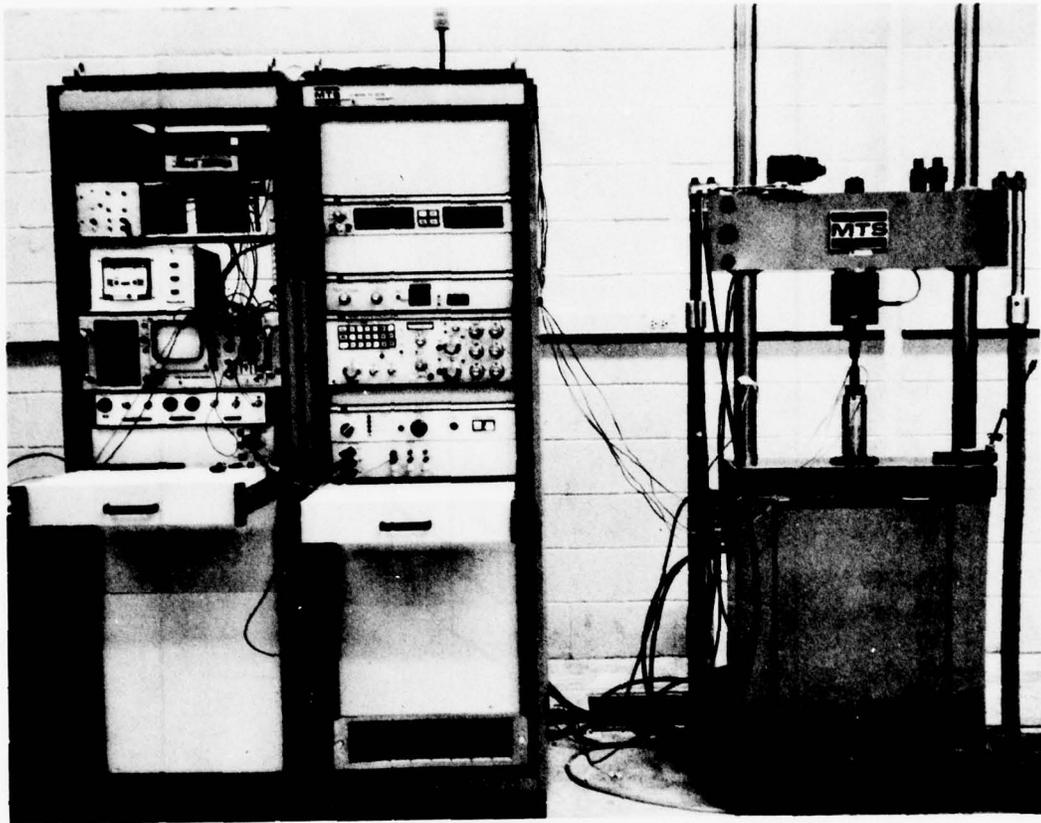
FIGURE 8. MTS MODEL 810 MATERIALS TEST SYSTEM.
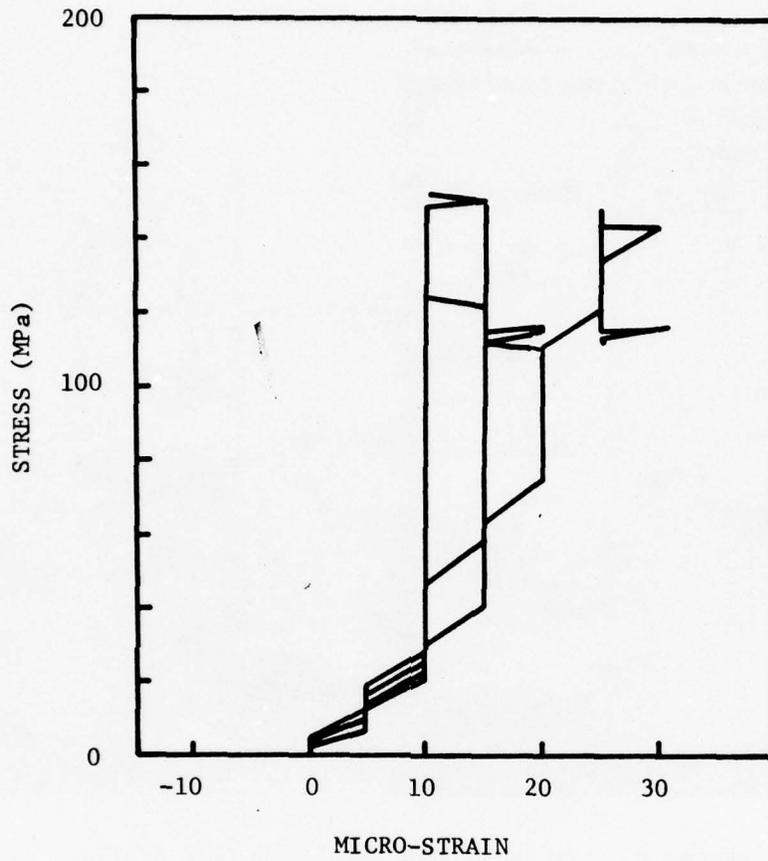
FIGURE 9. TYPICAL STRESS-STRAIN RELATIONS AS MEASURED
BY TRANSVERSE STRAIN GAGES ON ALL FOUR SIDES
OF A COMPRESSION SPECIMEN.   SPECIMEN C-1
(Z-DIRECTION).
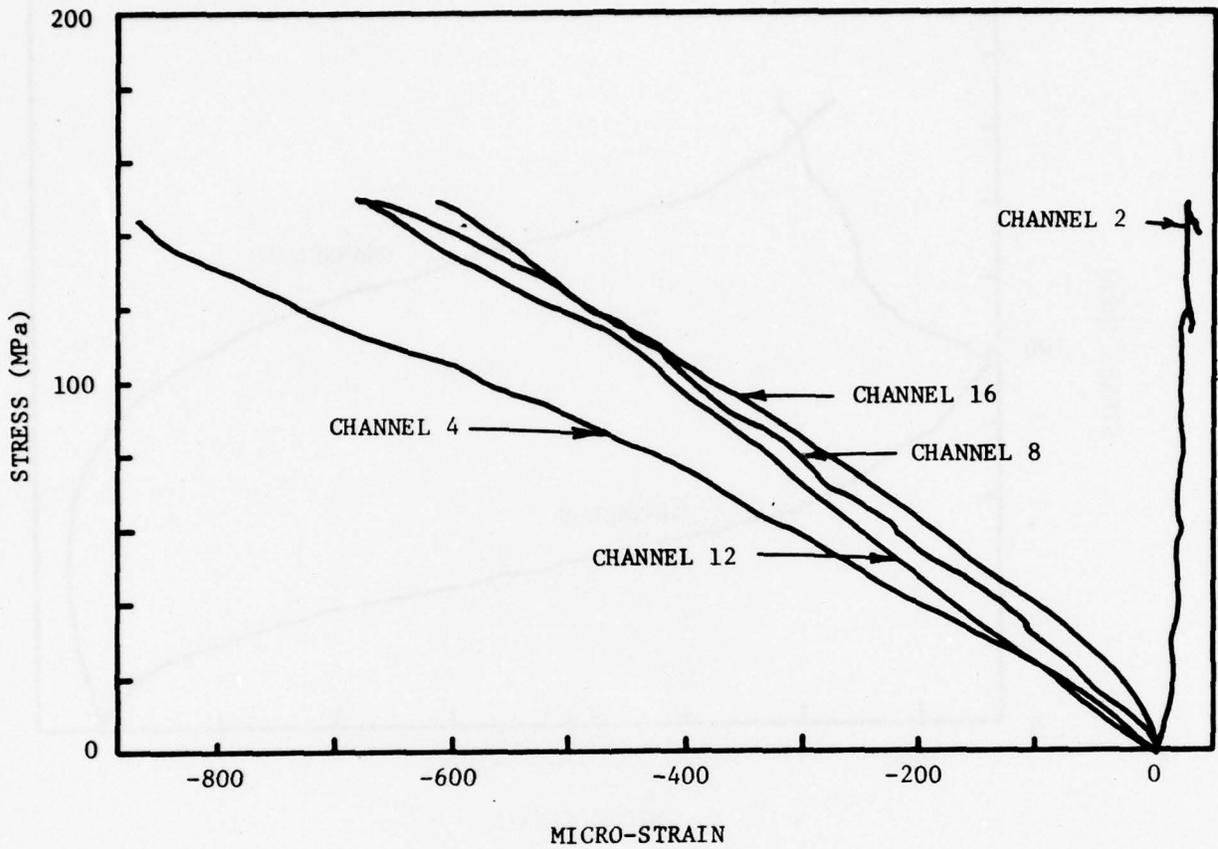
FIGURE 10. TYPICAL STRESS-STRAIN RELATIONS AS MEASURED
BY LONGITUDINAL STRAIN GAGES ON ALL FOUR
SIDES OF A COMPRESSION SPECIMEN. A TRANSVERSE
CHANNEL IS SHOWN FOR COMPARISON. SPECIMEN C-1
(Z-DIRECTION).
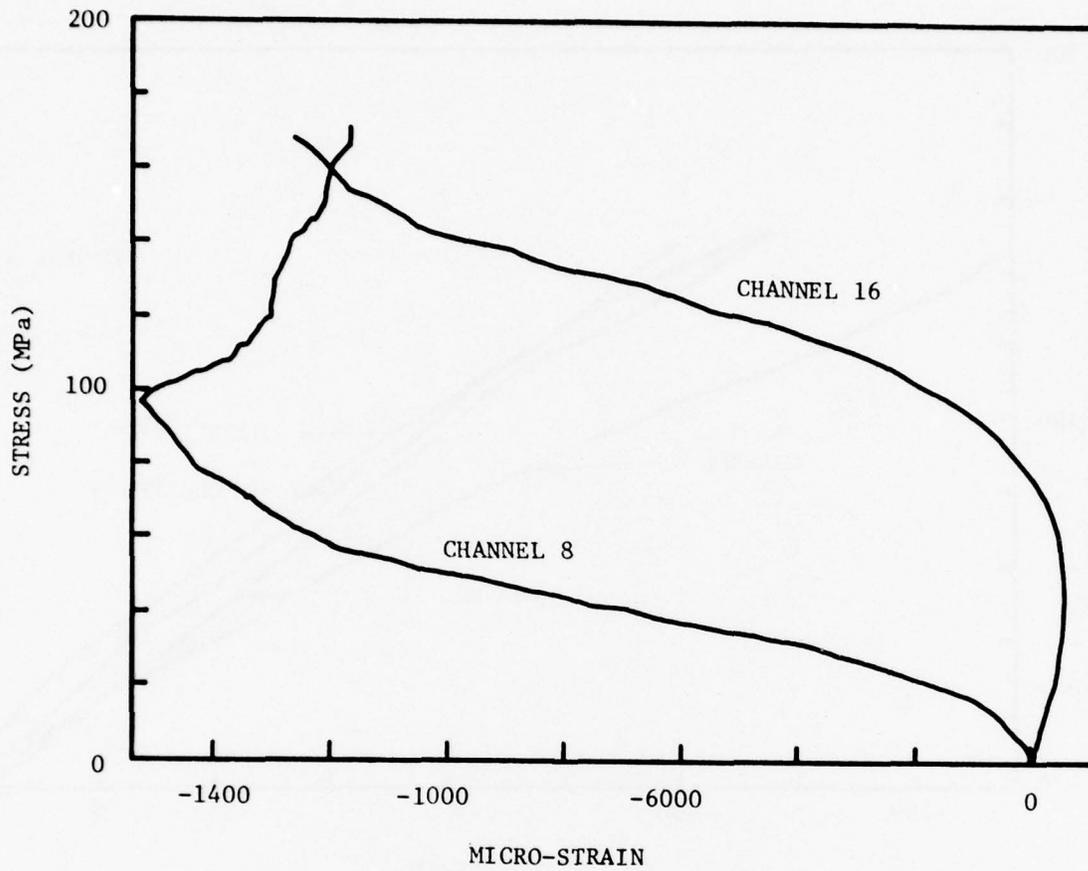
FIGURE 11.   STRESS-STRAIN RELATIONS FOR TWO GAGES
ON OPPOSITE SIDES OF A SPECIMEN WHICH
EXHIBITED CONSIDERABLE BENDING DURING
A COMPRESSION TEST.   SPECIMEN C-3
(Z-DIRECTION).

42
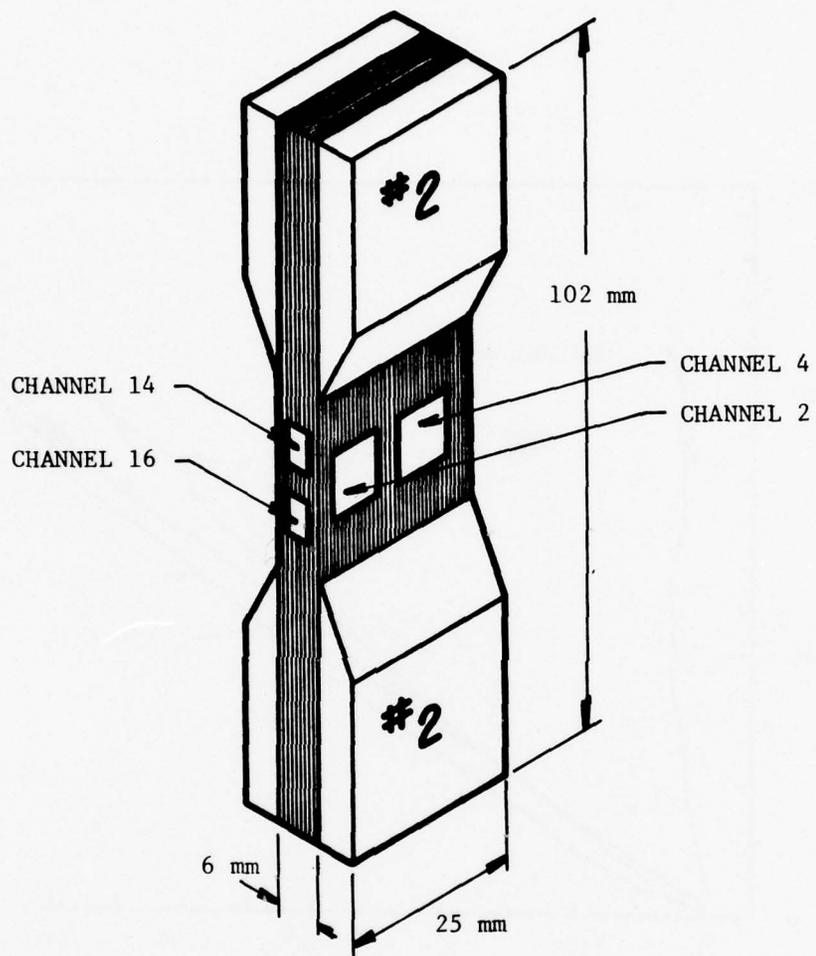
FIGURE 12. SKETCH OF TYPICAL TENSION SPECIMEN
WITH BIAXIAL STRAIN GAGES ON EACH
FACE.
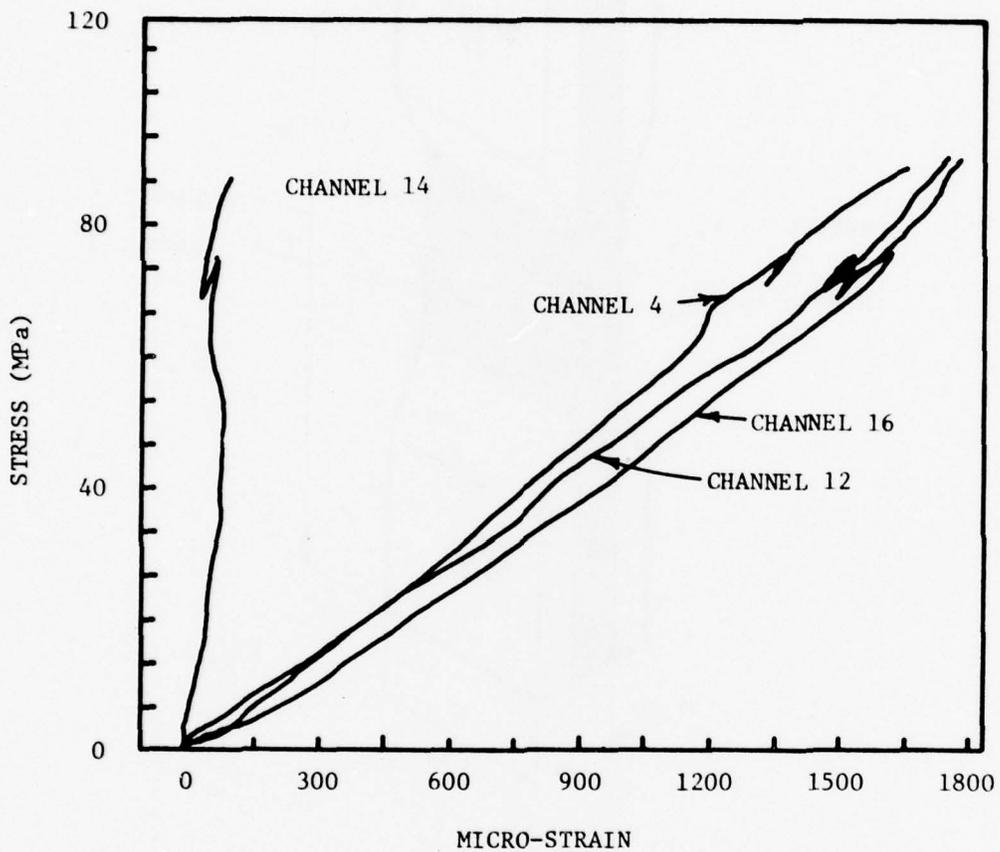
FIGURE 13. TYPICAL STRESS-STRAIN RELATIONS FOR THREE
LONGITUDINAL STRAIN GAGES (THE FOURTH GAGE
SHORTED OUT) ON A TENSILE SPECIMEN. A STRAIN
READING FROM A TRANSVERSE GAGE IS SHOWN FOR
COMPARISON (CHANNEL 14). SPECIMEN T-7
(Y-DIRECTION).

44
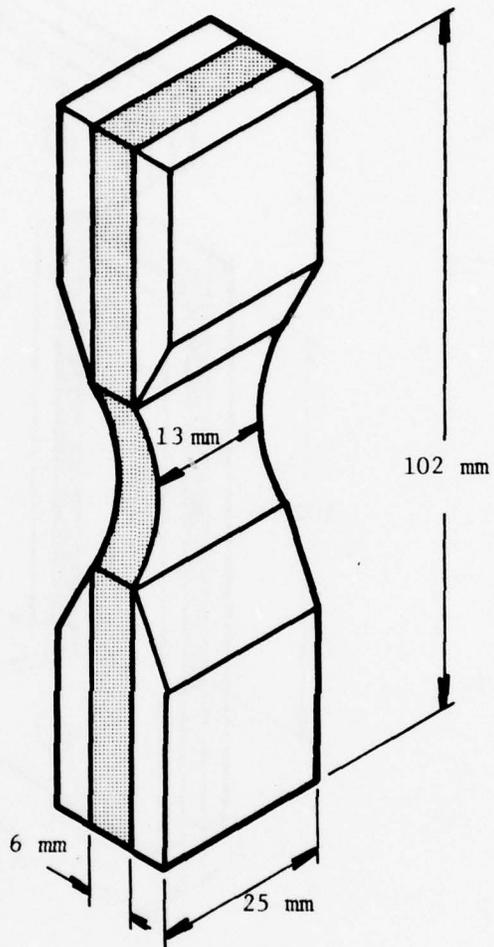
FIGURE 14. SKETCH OF TENSILE SPECIMEN WITH A
REDUCED CROSS-SECTIONAL AREA IN
THE CRITICAL TEST REGION.

45

FIGURE 15. SCHEMATIC DRAWING OF RAIL SHEAR SPECIMEN.

46

CENTER LINE

102 mm

6 mm

64 mm
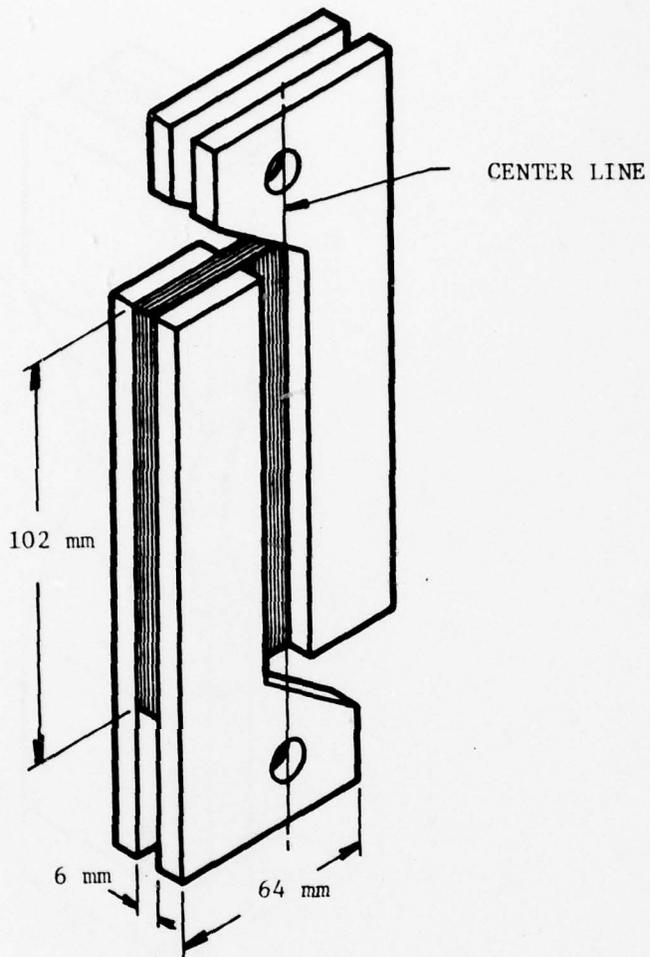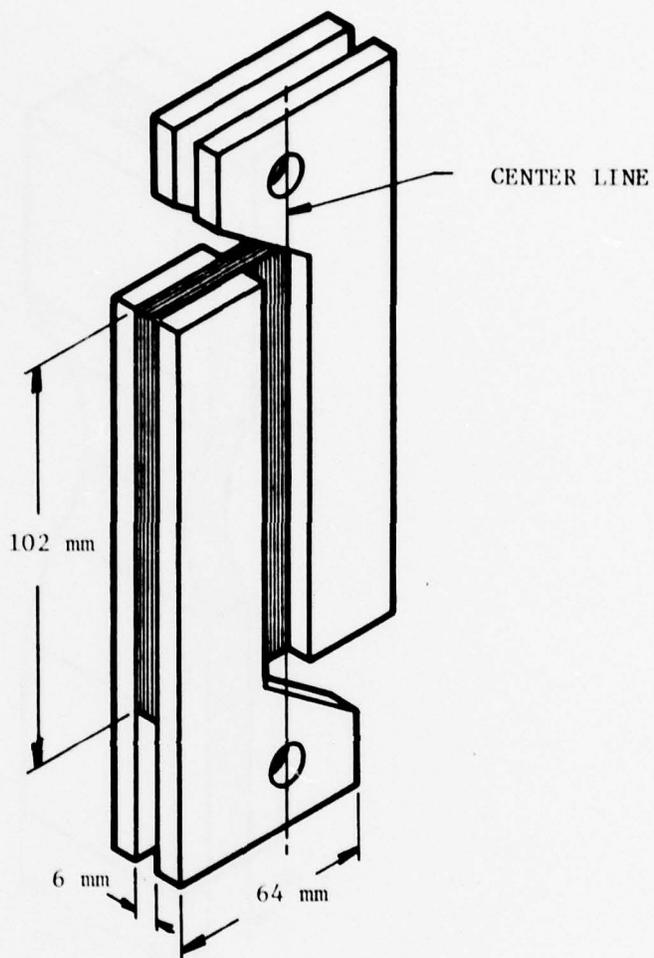
FIGURE 15. SCHEMATIC DRAWING OF RAIL SHEAR SPECIMEN.
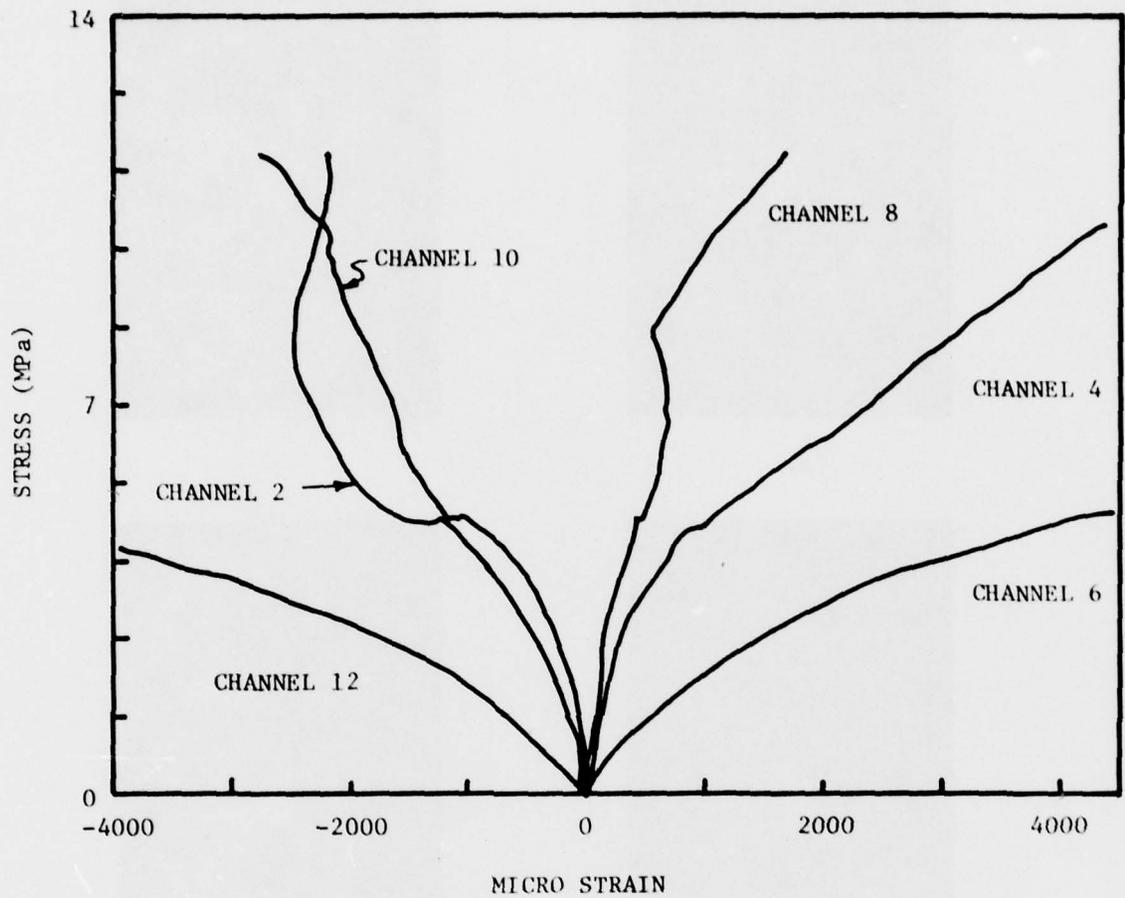
FIGURE 16. TYPICAL STRESS-STRAIN CURVES FOR RAIL SHEAR
TESTS. SPECIMEN S-6 (Y-DIRECTION) CHANNELS
2 AND 8 ARE STRAINS PERPENDICULAR; CHANNELS 4
AND 10 ARE PARALLEL; AND CHANNELS 6 AND 12
ARE ORIENTED AT 45° TO THE LOADING DIRECTION.
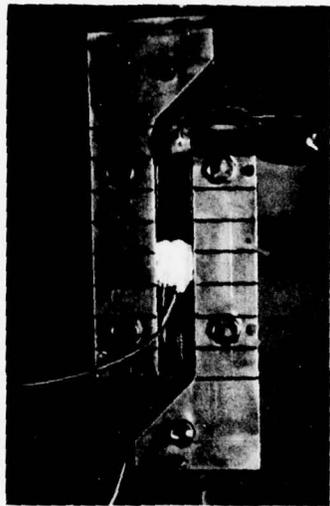
(a)
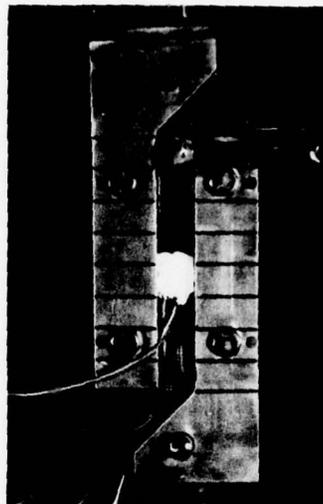
(b)
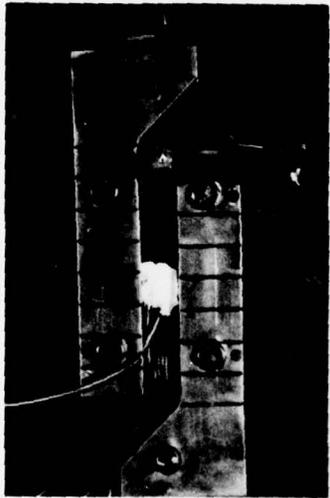
(c)

(d)

FIGURE 17.   LOADING SEQUENCE DURING RAIL SHEAR TEST.
SPECIMEN S-2:   00 MPa, 6.4 MPa (0.93 ksi),
14.4 MPa (2.09 ksi), 17.2 MPa (2.50 ksi).
ACOUSTIC EMISSION TRANSDUCER IS ATTACHED
TO THE TOP REGION OF THE SPECIMEN IN a,
b and c.

48
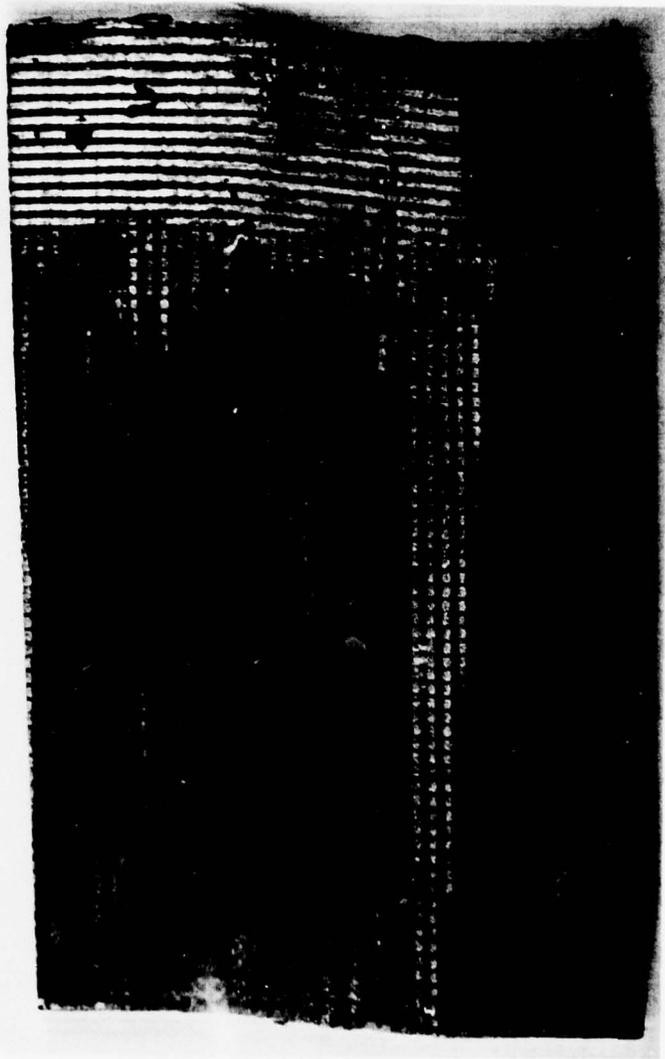
FIGURE 18.   SHEAR SPECIMEN AFTER TEST WAS RUN.   NOTE SUBSTANTIAL
AMOUNT OF PLASTIC DEFORMATION WHICH SPECIMEN SUSTAINED
WITHOUT CATASTROPHIC FAILURE.

(a)

T DIST. FROM T= 60   TO T= 90
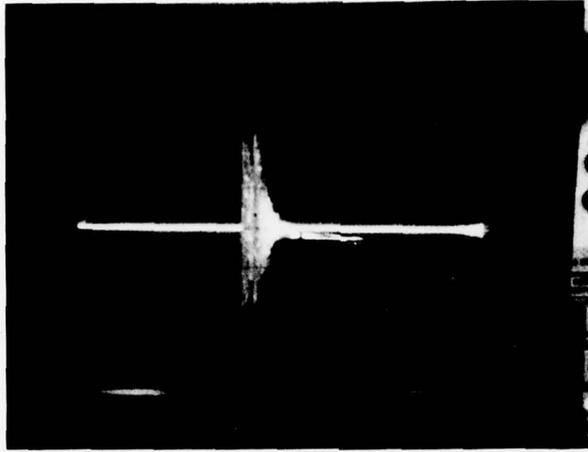
(b)

FIGURE 19.   PENTEL 0.5mm LEAD BREAK ON SPECIMEN C-24:
a) 0.2 VOLTS PER DIVISION - VERTICAL;
1 MILLISECOND PER DIVISION - HORIZONTAL,
150-400 KHz BANDPASS; 40 dB GAIN; b) COUNT
DISTRIBUTION GRAPH; 60 dB GAIN.

50
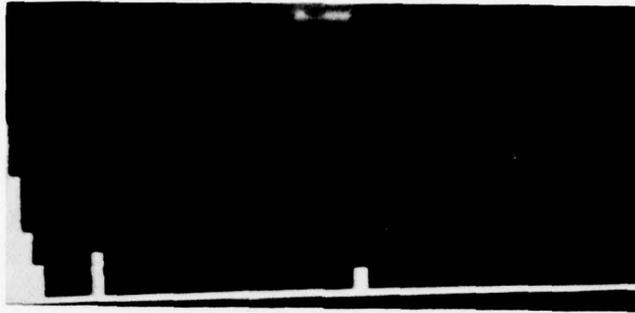
(a)
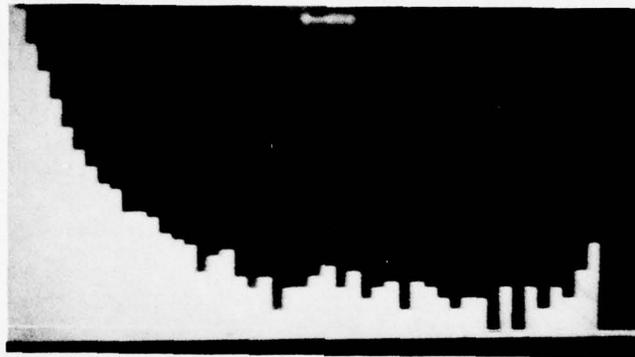
(b)
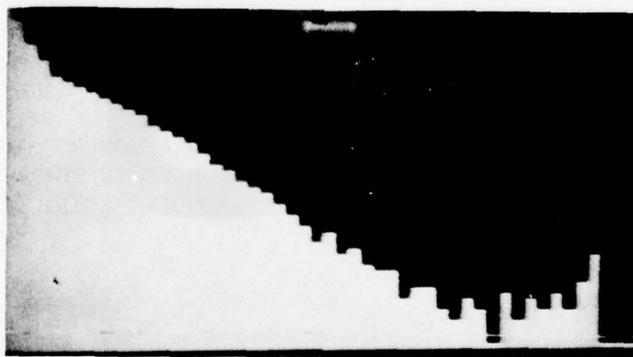
(c)

FIGURE 20.   COUNT DISTRIBUTION GRAPH, SPECIMEN C-10;
            40 dB GAIN: a) 46 MPa (6.67 ksi);
            b) 75 MPa (10.8 ksi); c) END OF TEST.
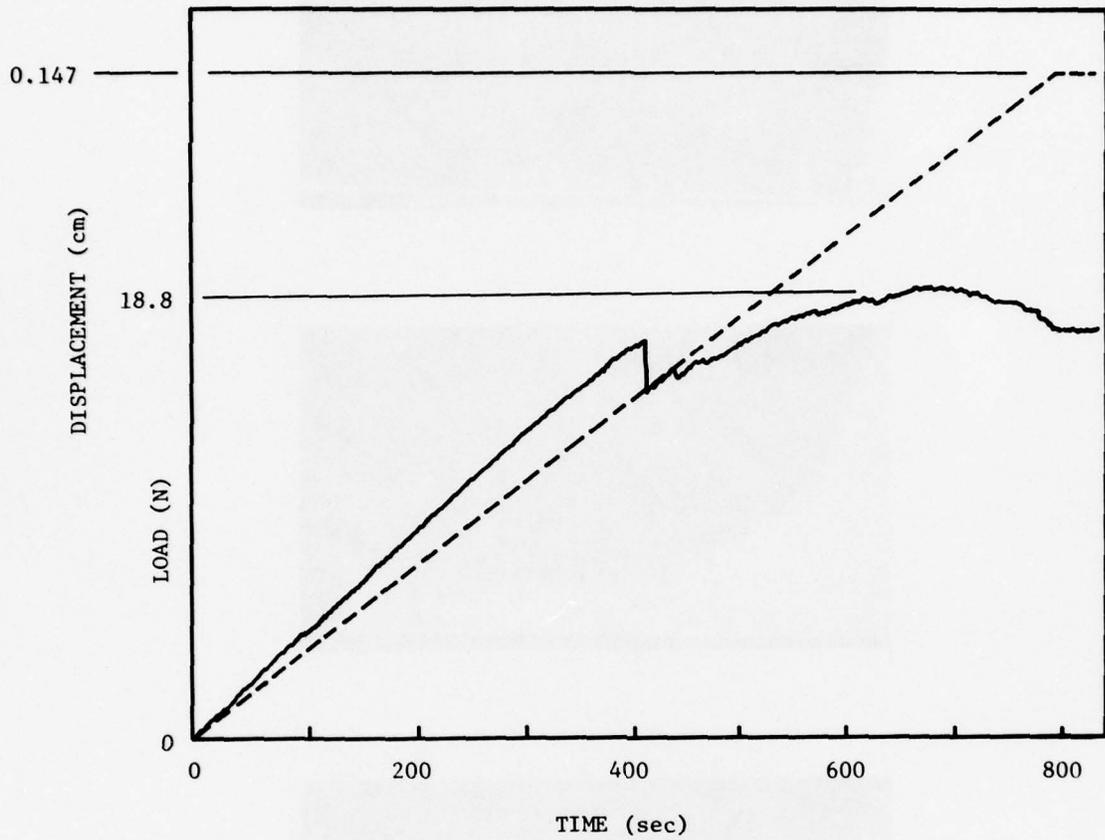
FIGURE 21. TYPICAL LOAD-DISPLACEMENT CURVE FOR A COMPRESSION TEST UNDER
DISPLACEMENT CONTROL.   THE BROKEN LINE IS THE DISPLACEMENT
AND THE SOLID LINE IS THE CORRESPONDING LOAD.   SPECIMEN C-19.

52
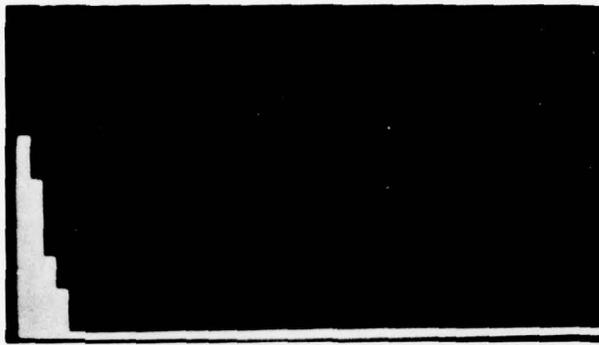
(a)
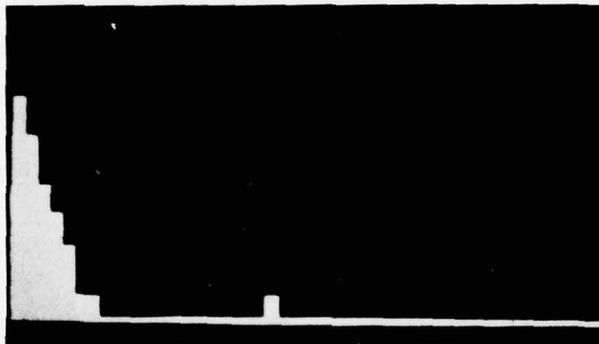
(b)
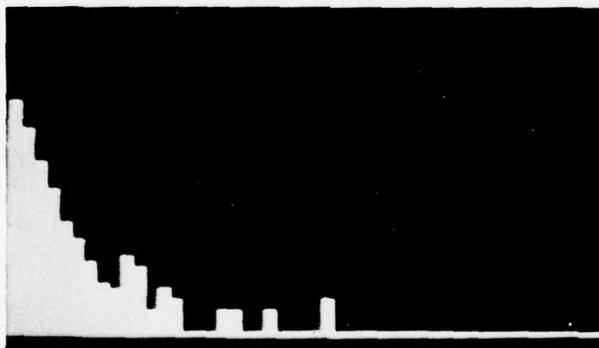
(c)

FIGURE 22.   AE COUNT DISTRIBUTION GRAPH FOR
SPECIMEN T-3.   40 dB GAIN: a)
53 MPa (7.8 ksi); b) 80 MPa
(11.6 ksi); c) 138 MPa (19.4 ksi),
END OF TEST.

53
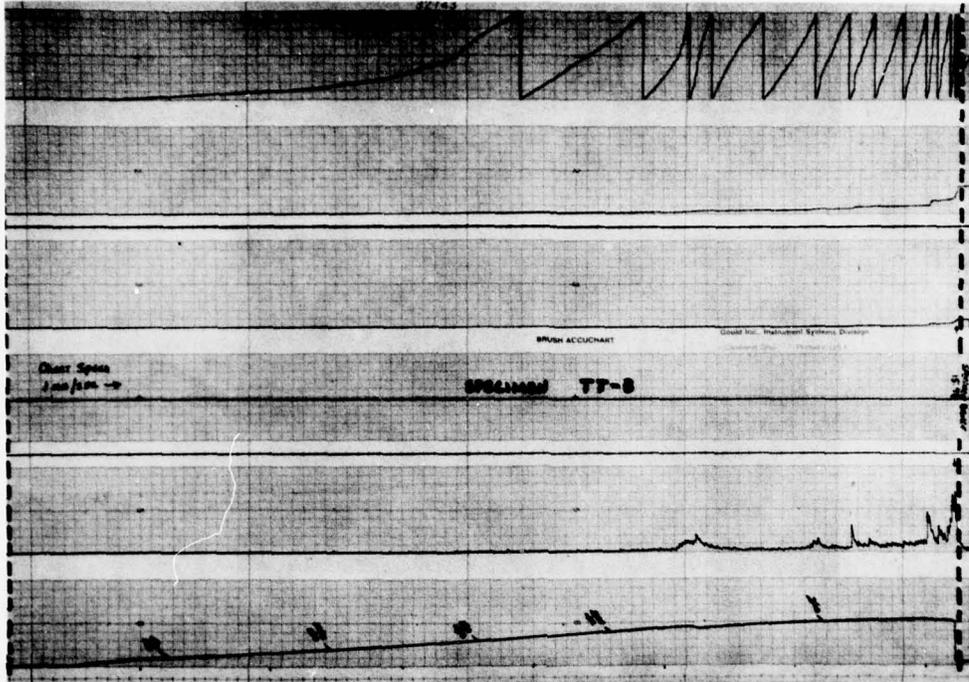
FIGURE 23. ACOUSTIC EMISSION DATA. BOTTOM CHANNEL
IS LOAD, 5000 POUND, FULL-SCALE. SECOND
CHANNEL IS COUNT RATE WITH 10 mV THRES-
HOLD; FULL SCALE IS 5V. CHANNELS 4-6
ARE ACCUMULATED RING-DOWN COUNTS WITH
THRESHOLDS OF 400 mV, 100 mV AND 10 mV,
RESPECTIVELY; FULL SCALE IS 65,536
COUNTS. (SPECIMEN TT-3)
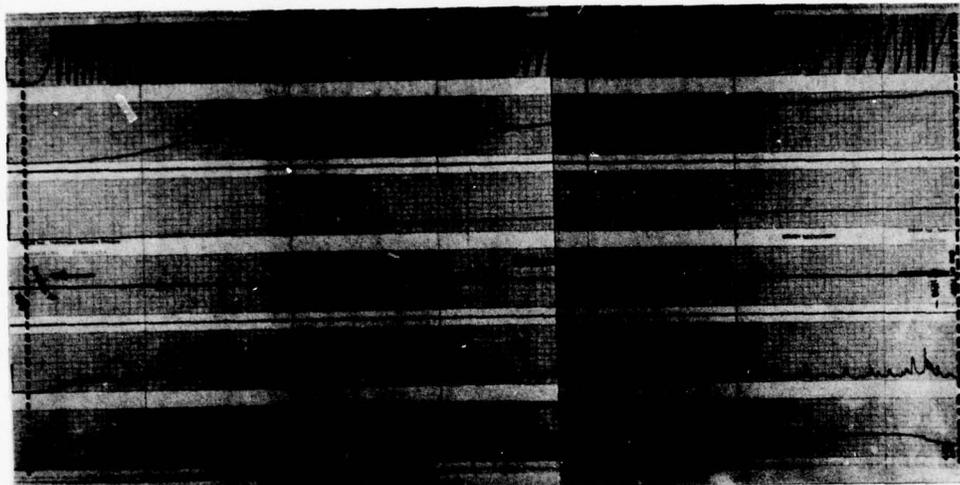
FIGURE 24.   FIVE CHANNEL RECORDING OF AE DATA
(SEE FIGURE 23 FOR DETAILS) FOR
SHEAR SPECIMEN (#S-7).

FIGURE 25. TYPICAL PHENOMENON SEEN IN SHEAR SPECIMENS (SPECIMEN S-7). PIN HOLES WERE USED TO PUT PRESSURE AGAINST SHEAR GRIPS IN ORDER TO ACHIEVE BETTER ADHESION WITH SPECIMENS.
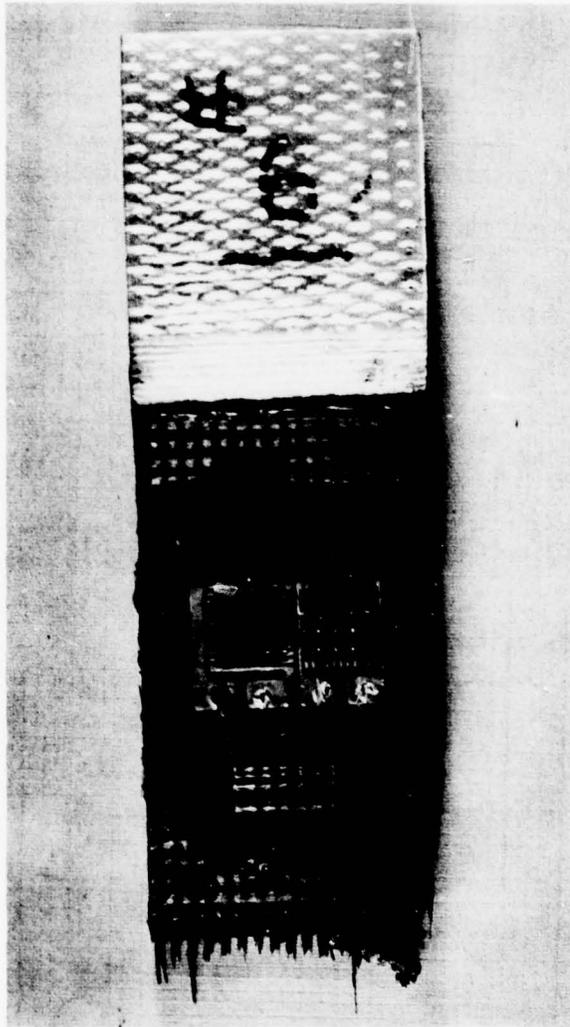
FIGURE 26. FAILED TENSILE SPECIMEN (SPECIMEN T-6)
SHOWING VERY LOCALIZED FIBER FRACTURE.
ORIENTATION OF THE SPECIMEN IS Y, Z, X
(Y-BUNDLES ALONG THE LENGTH, TENSILE
AXIS; Z-BUNDLES ACROSS THE WIDTH; AND
X-FIBER BUNDLES THROUGH THE THICKNESS).
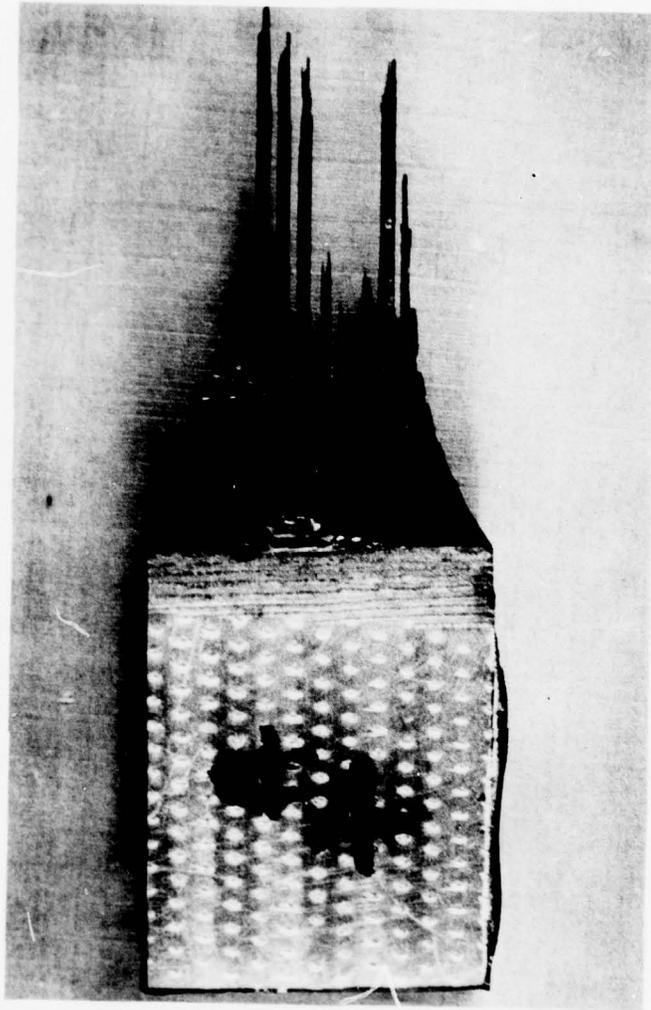
FIGURE 27. FAILED TENSILE SPECIMEN (T-4) SHOWING RANDOM
FIBER FAILURE LOCATION. ORIENTATION OF
SPECIMEN IS Z, Y, X.
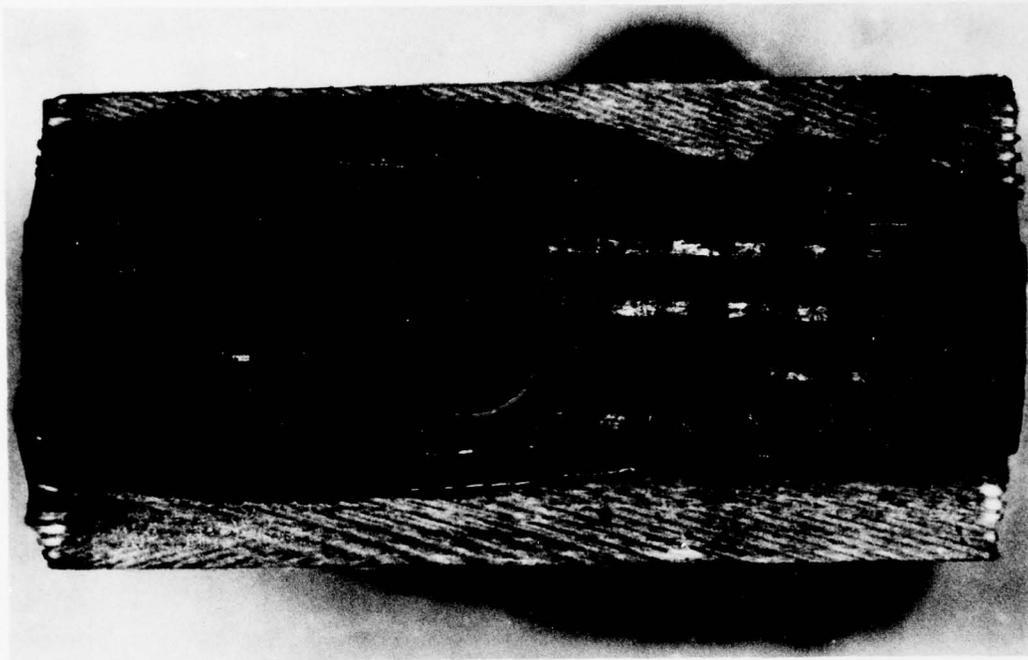
FIGURE 28. FAILED TENSILE SPECIMEN (SPECIMEN T-4) SHOWING LONGITUDINAL
FIBERS WHICH HAVE PULLED OUT OF SURROUNDING MATRIX AND
TRANSVERSE FIBER BUNDLE REGIONS, AT THE END OF THE SPECI-
MEN. SPECIMEN IS FOUR UNIT CELLS THICK.
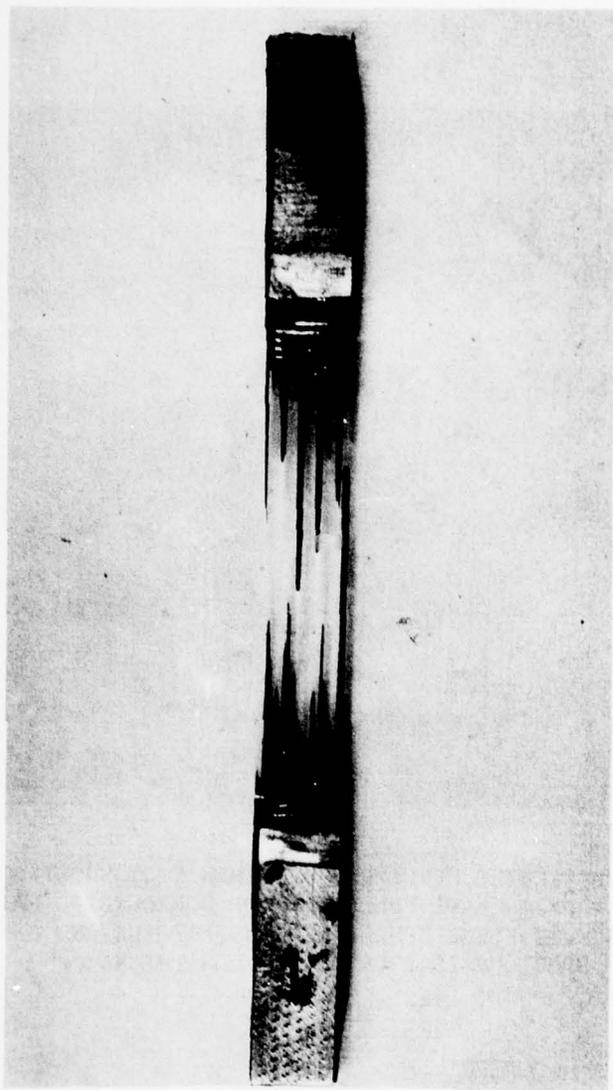
FIGURE 29. FAILED TENSILE SPECIMEN (SPECIMEN TT-1)
SHOWING SOME FIBERS WHICH PULLED COM-
PLETELY OUT OF THE SURROUNDING STRUCTURE.
SPECIMEN IS TWO UNIT CELLS THICK.

FIGURE 30. FAILED COMPRESSION SPECIMEN (SPECIMEN C-24)
SHOWING BROOMING PHENOMENON.

61
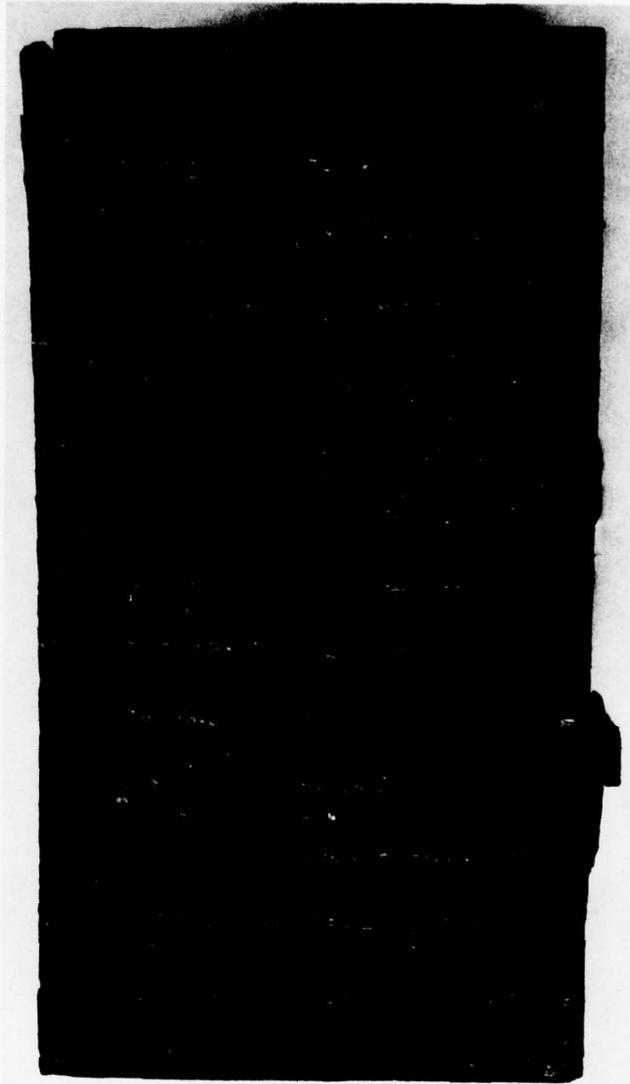
FIGURE 31. FAILED COMPRESSION SPECIMEN (SPECIMEN C-19)
SHOWING NORMAL DISPLACEMENT OF TRANSVERSE
FIBER BUNDLES.
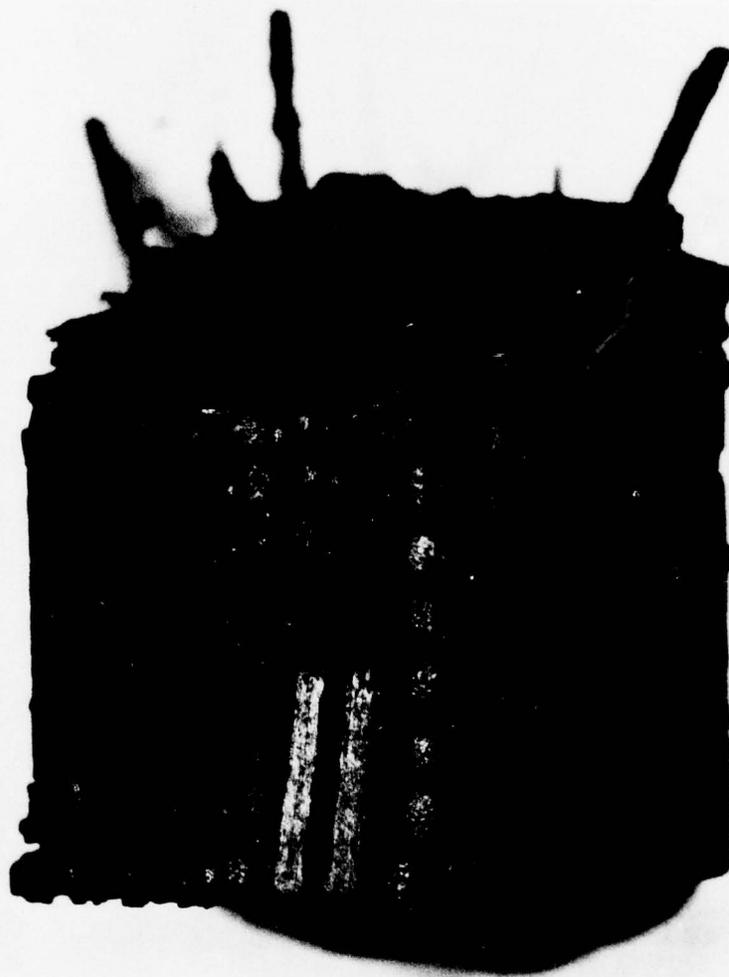
FIGURE 32. FAILED COMPRESSION SPECIMEN (SPECIMEN C-20, Y-DIRECTION)
SHOWING SHEAR-LIKE FAILURE SURFACE. FAILURE PLANE IS AT
AN ANGLE OF 25° TO 30° FROM PLANE NORMAL TO LOADING
DIRECTION. TEST TEMPERATURE WAS 1370°C (2500°F).
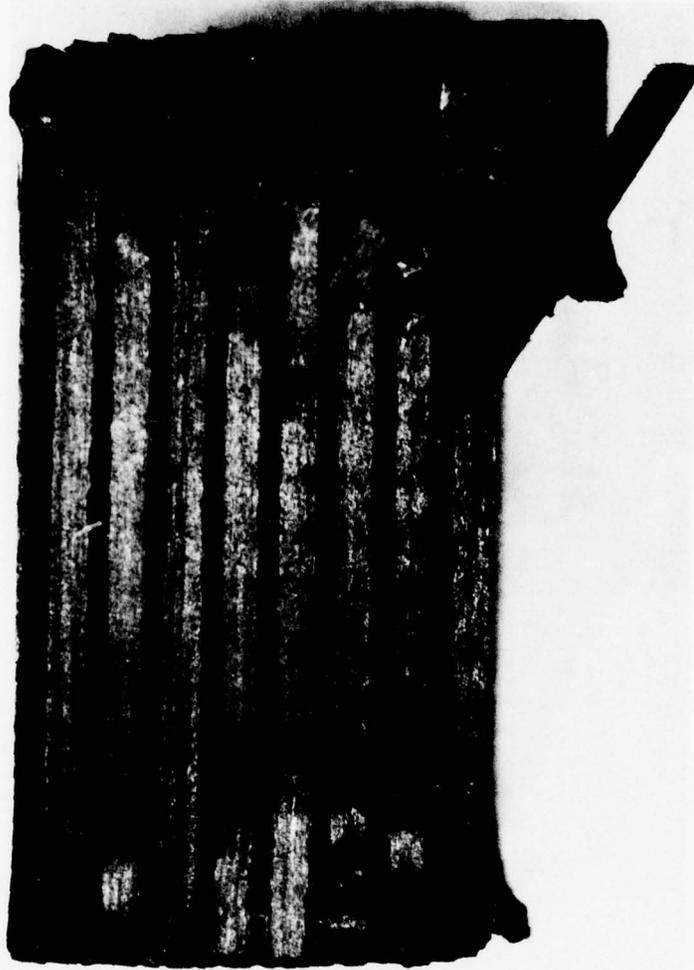
FIGURE 33.   FAILED COMPRESSION SPECIMEN (SPECIMEN C-11,
             Z-DIRECTION) SHOWING SHEAR-LIKE FAILURE.
             TEST TEMPERATURE WAS 1930°C (3500°F).
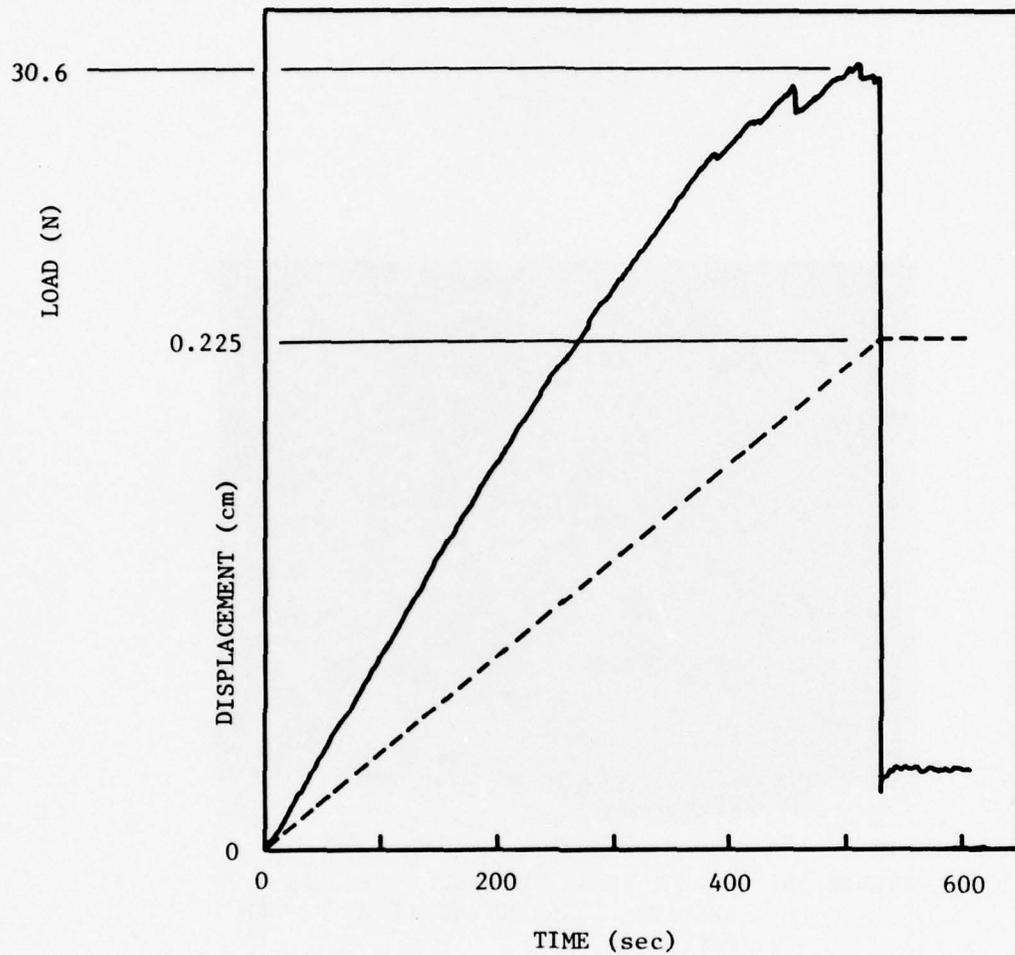
FIGURE 34. LOAD VERSUS DISPLACEMENT CURVE FOR HIGH TEMPERATURE
(1930°C, 3500°F) COMPRESSION TEST, SHOWING SUDDEN,
CATASTROPHIC FAILURE. THE BROKEN LINE IS DISPLACE-
MENT AND THE SOLID LINE IS THE CORRESPONDING LOAD.
(SPECIMEN C-11, Z-DIRECTION).
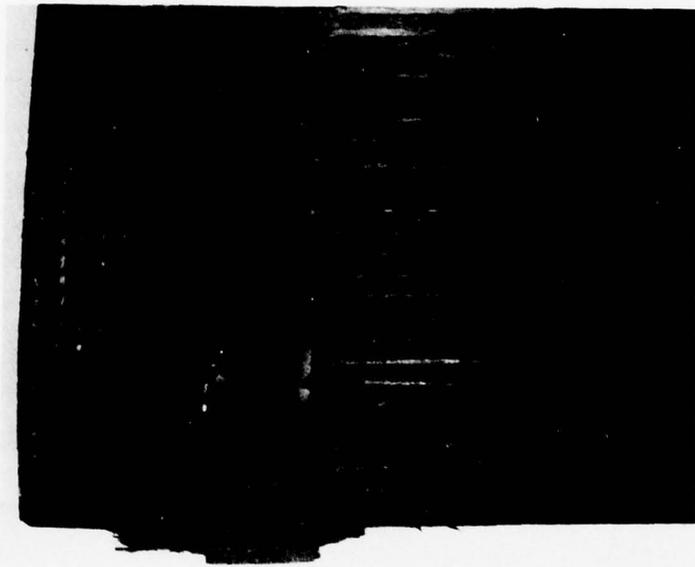
FIGURE 35.   FAILED SHEAR SPECIMEN (SPECIMEN S-2)
SHOWING LOCALIZED DAMAGE AT PINNED
HOLE.
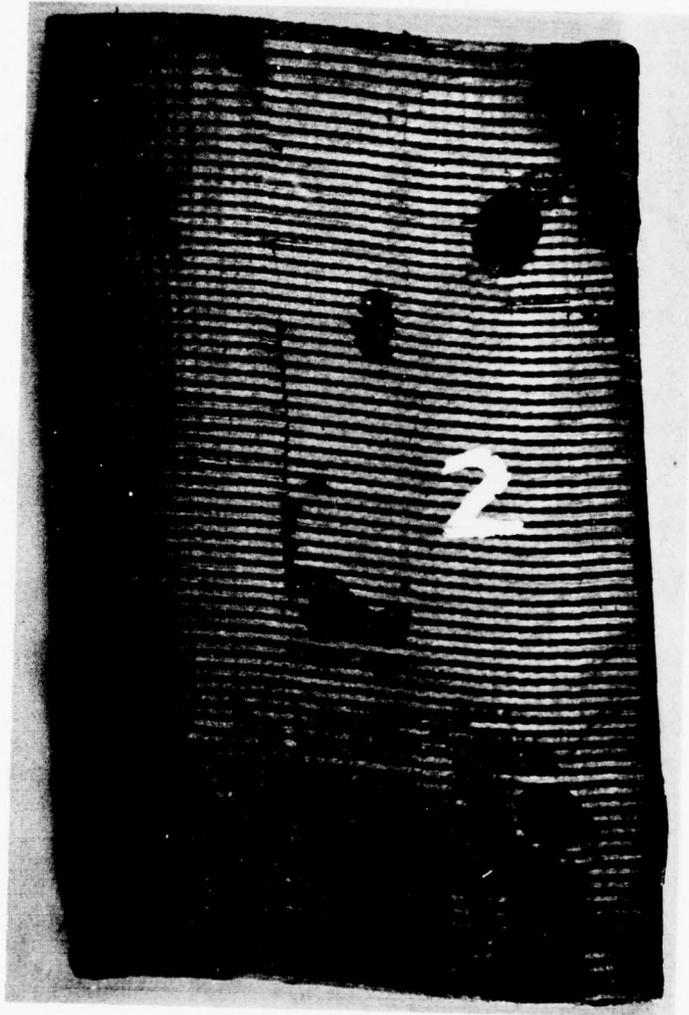
FIGURE 36.   FAILED SHEAR SPECIMEN (SPECIMEN S-2)
            SHOWING LARGE AMOUNT OF PLASTIC
            DEFORMATION.
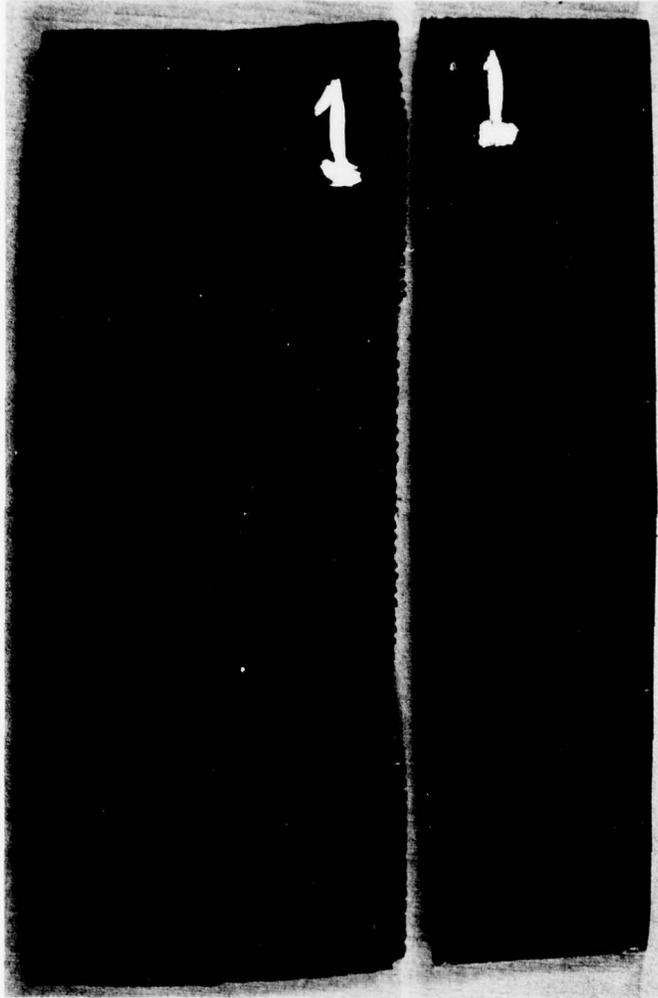
FIGURE 37.   FAILED SHEAR SPECIMEN (SPECIMEN S-1)
SHOWING UNUSUAL PHENOMENON OF
"BRITTLE" FAILURE.
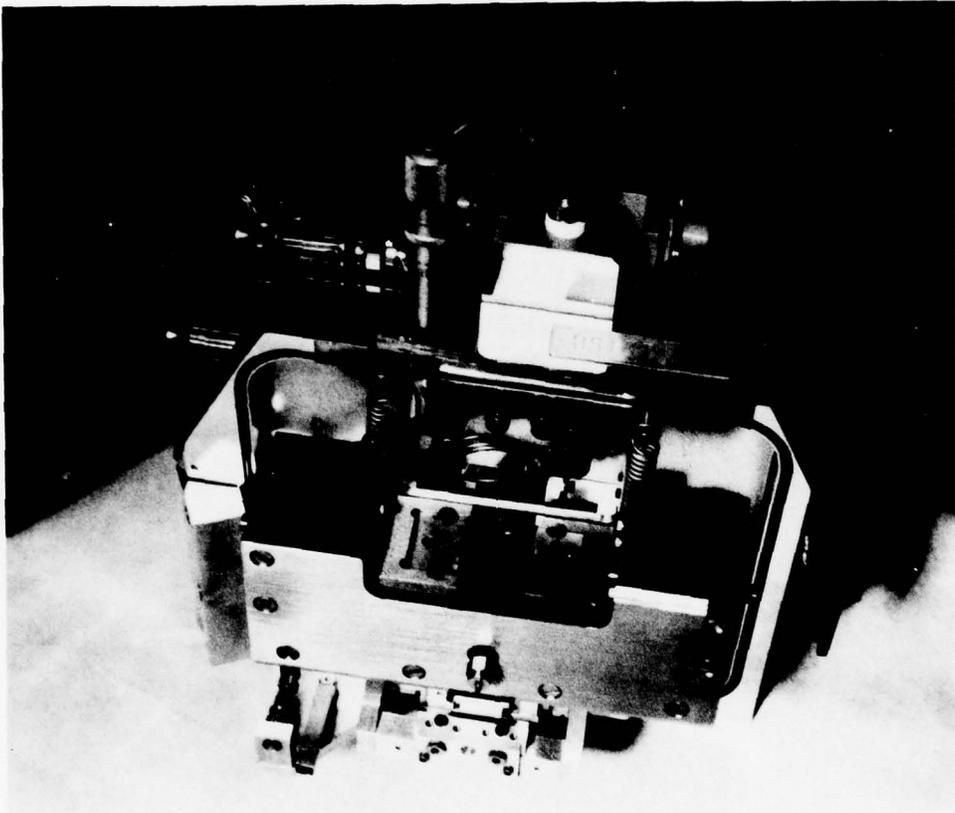
FIGURE 38.   LOADING STAGE FOR ETEC AUTOSCAN
SCANNING ELECTRON MICROSCOPE.
CARBON-CARBON SPECIMEN IS SHOWN
LOADED IN STAGE.

FIGURE 39. TYPICAL SEM SPECIMEN. LOAD IS
TRANSMITTED THROUGH THE EDGE
NOTCHES IN THE TABS. THE CENTER
HOLES ARE MERELY FOR ALIGNMENT
PURPOSES.

FIGURE 40. SEM PHOTOGRAPH (SPECIMEN SEM-14) SHOWING CRACK
WHICH INITIATED IN SHEAR (WHITE ARROW), PROPAGATED
OPENING MODE, AND FINALLY TURNED 90° (TO SHEAR
MODE AGAIN) AND RAN ALONG FIBER BUNDLE. 120X.
73 MPa (10.5 ksi). (LOADING DIRECTION IS OUT-
WARD IN HORIZONTAL DIRECTION).
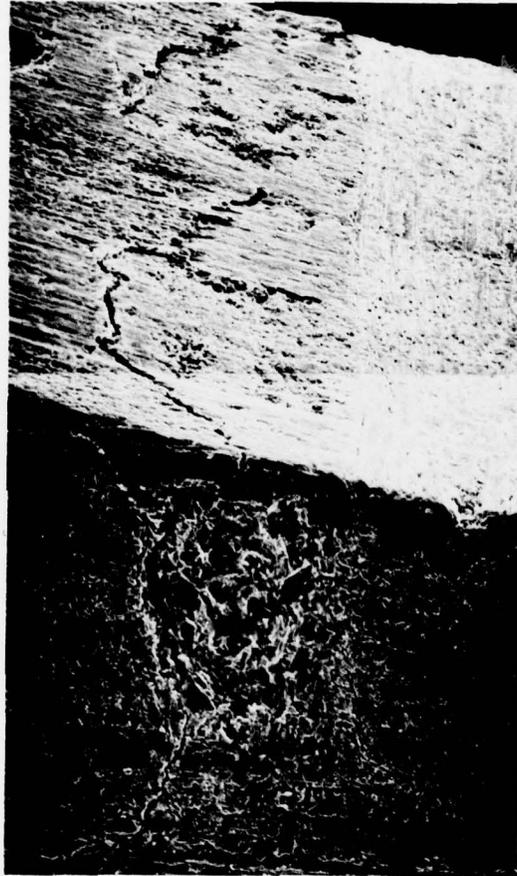
FIGURE 41. SEM PHOTOGRAPH (SPECIMEN SEM-14)
SHOWING CRACK RUNNING ACROSS TOP
EDGE AND DOWN FRONT FACE OF
SPECIMEN. 60X, 76 MPa (11.0 ksi).
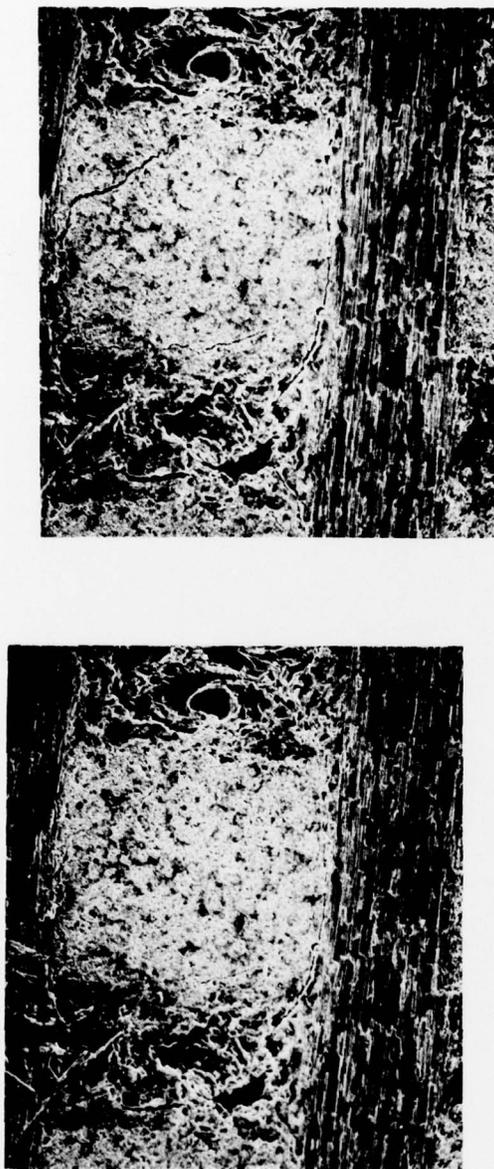
FIGURE 42. STEREO PAIR OF CRACK NETWORK (SPECIMEN SEM-20). 40X, 15.9 MPa (2.30 ksi) FOR 42(a) and 66.2 MPa (9.60 ksi) FOR 42(b). HORIZONTAL DISPLACEMENT DIFFERENCES WILL APPEAR AS NORMAL DISPLACEMENTS WHEN STEREO PAIR IS CORRECTLY ALIGNED.

FIGURE 43.   FAILED SEM SPECIMEN (SPECIMEN SEM-20), AT 17X.
STARTER NOTCH (TOP OF SPECIMEN) PASSED THROUGH
TOP FIBER BUNDLE.
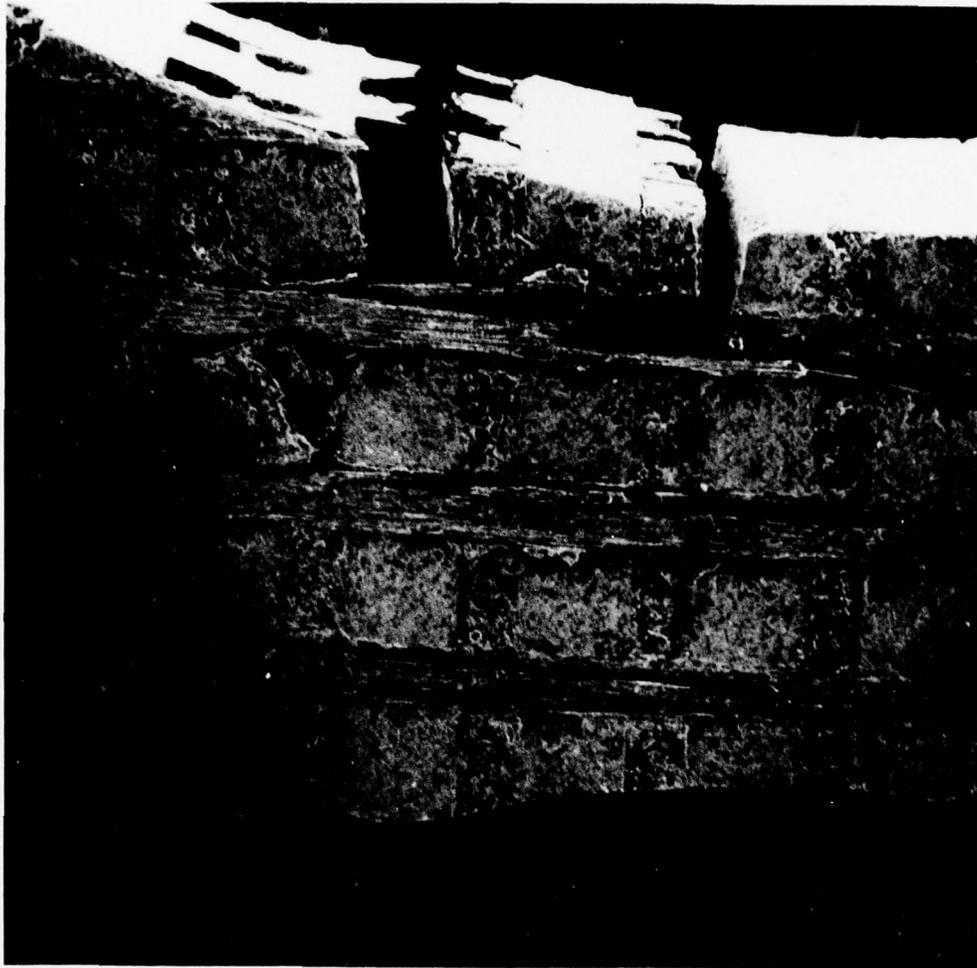
FIGURE 44.   FAILED SEM SPECIMEN (SPECIMEN SEM-21), AT 17X.
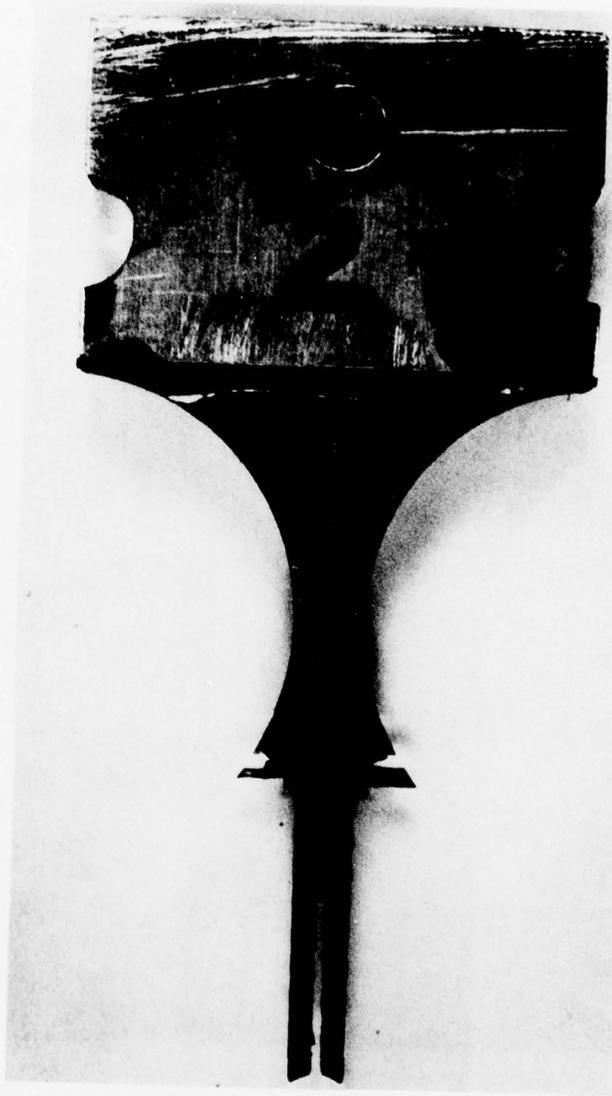
FIGURE 45. FAILED SEM SPECIMEN (SPECIMEN SEM-2, Z-DIRECTION).

FIGURE 46.   FAILED SEM SPECIMEN (SPECIMEN SEM-18,
             Y-DIRECTION).

APPENDIX A

DENSIFICATION ROUTING SHEET

Date Started: ~~August 25, 1977~~ Finished   Date Finished: 11/27/77

FMI P/N: _____ 2696 _____ Dimensions (in)   Preform Density: _____ .804 g/cc

Operation/Date	Dimensions			Weight (gms)	Volume	Density gms/cc	Approval, Remarks
	X	Y	Z				
Preform Density 8/25/77	4.290	4.289	8.571	2078	2585	.804	
Radiographic Insp.							
Fixturing (Graphite Cage)	Frame No. 696			2956			
1st Pitch Impreg. & Carb. 9/06/77	4.306	4.311	8.976	2871	2731	1.05	
1st 5000 PSI PIC 9/09/77	4.344	4.334	8.924	3440	2753	1.25	
1st Graphitization (2600°) 9/12/77	4.321	4.337	8.960	3335	2752	1.21	
Skin Machined 9/13/77	4.179	4.184	8.333	3056	2391	1.28	
2nd 5000 PSI PIC 9/16/77	4.210	4.207	8.378	3514	2432	1.44	
2nd Graphitization (2600°) 9/19/77	4.201	4.185	8.375	3.453	2413	1.43	
3rd 5000 PSI PIC 9/22/77	4.196	4.207	8.362	3862	2420	1.60	
3rd Graphitization (2600°) 9/26/77	4.208	4.200	8.370	3815	2424	1.57	
4th 5000 PSI PIC 9/29/77	4.214	4.201	8.391	4117	2435	1.69	
4th Graphitization (2600°) 10/03/77	4.215	4.204	8.386	4085	2435	1.68	
5th 5000 PSI PIC 10/7/77	4.237	4.250	8.395	4302	2478	1.74	
5th Graphitization (2600°) 10/10/77	4.233	4.222	8.380	4267	2455	1.74	

APPENDIX A (Cont'd)

DENSIFICATION ROUTING SHEET (cont'd)

FMI P/N: 2696 (cont.)

Operation/Date	Dimensions (in)			Weight (gms)	Volume	Density gms/cc	Approval/ Remarks
	X	y	Z				
6th 5000 PSI PIC 10/13/77	4.222	4.224	8.378	4476	2449	1.83	☺
6th Graphitization (2600°) 10/17/77	4.250	4.236	8.395	4452	2477	1.80	☺
1st Proprietary Cycle 10/21/77	4.217	4.232	8.370	4593	2448	1.88	☺
7th Graphitization 10/24/77	4.225	4.237	8.374	4592	2457	1.87	☺
2nd Proprietary Cycle 10/28/77	4.229	4.246	8.375	4660	2465	1.89	☺
8th Graphitization 10/31/77	4.236	4.256	8.376	4660	2475	1.88	☺
.achined 11/16/77	4.165	4.175	8.172	4383	2329	1.88	Lowell
3rd Proprietary Cycle 11/22/77	4.171	4.174	8.180	4430	2334	1.90	
9th Graphitization 11/28/77	4.170	4.170	8.176	4428	2330	1.90	

Ray V. Carpenter
In-Process Quality Control

80

A low-frequency cyclic-loading stage for the SEM

D L Davidson and A Nagy
Southwest Research Institute, 8500 Culebra Road, San Antonio, Texas 78284, USA

Abstract A cyclic-loading stage for the ETEC Corporation SEM is described. The stage uses servo-controlled electro-hydraulic loading with positive feedback. Specimens are loaded symmetric to the specimen centre line. Maximum load is 4893 N, with a maximum loading rate of 4 Hz. Resolution on the specimen is about 50·0 nm for static observation and 100·0 nm for dynamic (TV rate) observation in the secondary-electron mode. Observation of the specimen may also be made using backscattered electrons, and in the channelling mode (channelling patterns and channelling contrast). Maximum specimen motion during cyclic loading is 15 μm.
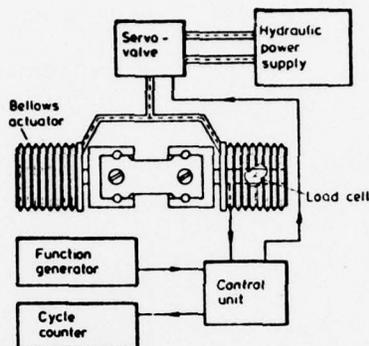
Figure 1 Diagram of loading and control system.

Figure 2 Loading system assembly with specimen.

Figure 5 Diagram of control system.

DOD

Office of the Secretary of Defense
Director of Defense Research and
   Engineering
       OAD/OS/Mr. B. Barse
       OAD/ET/Mr. J. Persh
       OAD/SW/Dr. R. Ruffine
Washington, DC 20301

Plastics Technical Evaluation
  Center, Building 176
ATTN: Mr. A. Anazione
Department of Defense
Picatinny Arsenal
Dover, NJ 07801

AIR FORCE

Air Force Materials Laboratory
AFML/
      CC/Dr. F. Kelley
      MB/Mr. J. Kelble
      MBC/Dr. R. Craig
      MBC/Dr. W. Kessler
      MBC/Mr. D. Schmidt
      MBM/Dr. N. Pagano
      MX/Dr. M. Minges
      MXE/Lt. T. Curci
      MXE/Capt. E. Heinonen
      MXE/Mr. J. Latva
      MXE/Mr. G. Ormbrek
      MXE/Lt. G. Wendt
      LTN/Mr. H. Materne
Wright-Patterson AFB, OH 45433

Air Force Office of Scientific Research
AFOSR/NC/Dr. D. Ulrich
      NC/Dr. D. Ball
      NC/Dr. W. Walker/Dr. C. Hays
      L/COL R. Haffner
Building 410
Bolling AFB, DC 20332

Air Force Rocket Propulsion Laboratory
AFRPL/
      MK/Dr. C. Hawk
      MKC/Mr. L. Tepe
      MKCC/Mr. W. Payne
      CA/Mr. R. Weiss
Edwards AFB, CA 93523

Air Force Weapons Laboratory
AFWL/
      Lt. Col. D. Ericson
Kirtland AFB, NM 87117

SAMSO/ABRES
ATTN: Lt. Col. J. McCormack
Worldway Postal Center
P. O. Box 92960
Los Angeles, CA 90009

Space and Missile Systems
SAMSO/
      MNNR/Capt. T. Brocato
      MNPX/Capt. D. Bailey
Norton AFB, CA 92409

ARMY

Army Materials and Mechanics Research
      Center
ATTN: AMXMR-H/J. Dignam
Watertown, MA 02172

NAVY

Assistant Secretary of the Navy (R&D)
ATTN: Dr. S. Koslov
Washington, DC 20301

Office of the Chief of Naval Operations
ATTN: Mr. R. Blaise (OP-620E)
Department of the Navy
Washington, DC 20350

Director, Naval Research Laboratory
ATTN: Dr. S. Freiman/Mr. P. Mast
      (Code 8434)
Washington, DC 20375

Office of Naval Research
ATTN: Dr. A. Diness (Code 471)
800 North Quincy
Arlington, VA 20305

Commander, Naval Sea Systems Command, HQ.
ATTN: Mr. M. Kinna (SEA-0352)
      Dr. J. Huth (SEA-03C)
      Mr. G. Sorkin (SEA-035)
Washington, DC 20302

Commander
Naval Surface Weapons Center
      Mr. R. Edwards/Code WA-43
      Mr. R. Feldhuhn/Code WA-43
      Dr. W. Lyons/Code WA-07
      Mr. C. Rowe/Code WR-31
      Mr. J. Vamos
      Mr. J. Wagner/Code WA-43
      Mr. R. Wilson/Code WR-31
White Oak
Silver Spring, MD 20910

Commander
Naval Weapons Center
      Mr. J. Patton/Code 3161
      Mr. E. Jeter/Code 3162
China Lake, CA 93555

Director
Strategic Systems Project Office (PM-1)
ATTN: Dr. J. Kincaid/SP-20
      Dr. H. McMasters/SP-2723
      Mr. S. Weinger/SP
Department of the Navy
Washington, DC 20376

Project Manager
Trident Systems Project (CNM-PM 2)
ATTN: Mr. J. Crone/HM-2-001
Department of the Navy
Washington, DC 20360

NASA

NASA, Marshall Space Flight Center
ATTN: Mr. B. Powers, EP 25
Huntsville, AL 35812

DNA

Director, Defense Nuclear Agency
ATTN: Mr. D. Kohler
      Mr. J. Moulton
Washington, DC 20305

ERDA

U.S. Energy Research Division
  Administration
ATTN: Mr. A. Littman
Nuclear Research and Application Div.
Washington, DC 20331

INDUSTRY (OTHERS)

Acurex/Aerotherm
ATTN: Mr. H. Tong
      Mr. R. Manfred
      Mr. J. Dodson
      Mr. J. Zimmer
485 Clyde Avenue
Mountain View, CA 94042

Aerojet
ATTN: Mr. J. Cauzza
      Mr. H. Davis
      Mr. M. Clone
      Mr. R. Dona
P. O. Box 13400
Sacramento, CA 95813

Aeronutronic-Ford
ATTN: Mr. J. Perry
Ford Road
Newport Beach, CA 92663

Aerospace Corporation
ATTN: Dr. S. Batdorf
      Dr. H. Blaes
      Dr. S. Brelant
      Mr. J. Evangelides
      Dr. R. Hallse
      Mr. W. Herbig
      Dr. R. Meyer
      Mr. R. Mortensen
      Dr. L. Rubin
P. O. Box 92957
Los Angeles, CA 90009

Atlantic Research Corporation
ATTN: Mr. W. Armour
      Mr. J. Baetz
      Mr. J. Bird
      Mr. R. Brown
5390 Cherokee Avenue
Alexandria, VA 22314

Avco Corporation
ATTN: Mr. B. Benz
      Mr. G. Mullen
      Mr. A. Traverna
Lowell Industrial Park
Lowell, MA 01851

Avco Corporation
ATTN: Mr. P. Rolincik
201 Lowell Street
Wilmington, MA 01887

Battelle Memorial Institute
ATTN: Mr. W. Chard
505 King Avenue
Columbus, OH 43201

Boeing Company
ATTN: Mr. J. Bedwell
P. O. Box 3996/MS 88-19
Seattle, WA 98124

California Research and Tech., Inc.
ATTN: Dr. K. Kreynenhagen
6269 Dariel Avenue
Woodland Hills, California 91364

Carborundum Company
Graphite Products Division
ATTN: Mr. W. Carlson
2050 Cory Drive
Sanborn, NY 14132

Effects Technology, Inc.
ATTN: Mr. J. Green
      Mr. M. Graham
5383 Hollister Avenue
Santa Barbara, CA 93105

Mr. D. Ehrentreis
Dave Ehrentreis Consulting Engr.
5 Horizon Road
Ft. Lee, NJ 07024

Fiber Materials, Inc.
ATTN: Mr. L. McAllister
Biddeford Industrial Park
Biddeford, ME 04005

General Electric Co., RESD
ATTN: Mr. P. Bolinger
      Dr. J. Gebhardt
      Mr. K. Hall
      Mr. D. Lowe
      Dr. E. Stover
      Mr. W. Reiley
P. O. Box 7560 - Room 2023
Philadelphia, PA 19406

General Electric Co., RESD
ATTN: Mr. A. Levine
3198 Chestnut Street
Philadelphia, PA 19101

Great Lakes Carbon Corporation
ATTN: Mr. W. Benn
299 Park Avenue
New York, NY 10017

Great Lakes Research Corporation
ATTN: Mr. H. Gilliam
P. O. Box 1031
Elizabethton, IN 37643

HAVEG
ATTN: Mr. R. Pegg
      Mr. R. Rodriguez
12827 East Imperial Highway
Santa Fe Springs, CA 90670

Hercules Corporation
ATTN: Mr. P. Christensen
      Mr. K. Dickerson
      Mr. B. McKenzie
P. O. Box 93
Magna, UT 84044

HITCO
ATTN: Mr. L. Dyson
1600 West 135th Street
Gardena, CA 90249

Jet Propulsion Laboratory
ATTN: Mr. N. Kimmel
Pasadena, CA 91103

Kaiser
ATTN: Mr. M. Fischer
      Mr. W. Sidney
880 Doolittle Drive
San Leandro, CA 94577

Lawrence Livermore Laboratories
ATTN: Mr. A. Maimoni (L-503)
P. O. Box 808
Livermore, CA 94550

Lockheed Missiles and Space Company
ATTN: Mr. R. Greene
      Mr. G. Grunwald
      Mr. A. Johnson
      Mr. A. Mietz
      Dr. M. Steinberg
P. O. Box 504
Sunnyvale, CA 94088

Los Alamos Scientific Laboratory
ATTN: Mr. R. Imprescia
      Dr. J. Taylor & C. Stein
University of California
P. O. Box 1663
Los Alamos, NM 87545

Materials Sciences Corporation
ATTN: Dr. S. Chatterjee
       Dr. J. Kibler
       Dr. B. Rosen
Blue Bell Office Campus
Merion Towle Building
Blue Bell, PA 19422

McDonnell Douglas Astronautics Co.
ATTN: Mr. L. Greszczuk
       Mr. J. Jortner
       Mr. B. Leonard
       Dr. J. Peck
       Mr. A. Penton
       Mr. R. Seibold
5301 Bolsa Avenue
Huntington Beach, CA 92647

McDonnell Douglas Research Labs.
ATTN: H. Holman
P. O. Box 516
St. Louis, MO 63166

NETCO
ATTN: Mr. W. Pfeifer
       Ms. P. Sullivan
       Mr. R. Young
110 Pine Avenue, Suite 906
Long Beach, CA 90802

Prototype Development Associates, Inc.
ATTN: Mr. Alexander
       Dr. G. Crose
       Dr. J. McDonald
       Mr. G. Schutzler
1740 Garry Avenue, Suite 201
Santa Ana, CA 92705

Sandia Laboratories
ATTN: Mr. D. Northrup
P. O. Box 5800
Albuquerque, New Mexico 87115

Science Applications, Inc.
ATTN: Mr. F. Clayton
       Mr. D. Eitman
       Mr. K. Kratsch
       Dr. W. Loomis
       Mr. J. Pope
       Dr. P. Randles
201 West Dyer Road, Unit C
Santa Ana, CA 92707

Southern Research Institute
ATTN: Mr. C. Canada
       Mr. H. Littleton
       Mr. H. Starrett
       Mr. C. Pears
2000 Ninth Avenue, South
Birmingham, AL 35205

Southwest Research Institute
ATTN: Dr. Philip H. Francis
       Dr. J. Lankford
P. O. Drawer 28510
San Antonio, TX 78284

Stackpole Fibers Company, Inc.
ATTN: Mr. G. Flemming
Foundry Industrial Park
Lowell, MA 01852

Super-Temp Company
ATTN: Mr. D. Bauer
111205 Norwalk Boulevard
Santa Fe Springs, CA 90670

Systems, Science and Software
ATTN: Mr. C. Emde
       Dr. G. Gurtman
P. O. Box 1620
La Jolla, CA 92037

Thiokol
ATTN: Mr. G. Broman
       Dr. S. Kulkarni
       Mr. A. Canfield
       Mr. R. Laramee
Brigham City, UT 84302

TRW Systems Defense Space Systems
ATTN: Dr. W. Kotlensky
Building R-1-Room 2012
One Space Park
Redondo Beach, CA 90278

Union Carbide Corporation
Nuclear Division (Y-12 Plant)
ATTN: Mr. A. Taylor
       Dr. G. Weber
P. O. Box Y
Oak Ridge, TN 37839

Union Carbide Corporation
Carbon Products Division
ATTN: Mr. J. Bowman
       Dr. J. Criscione
P. O. Box 6116
Cleveland, OH 44101

United Technologies
Chemical Systems Division
ATTN: Mr. R. Ellis
       Mr. P. O'Driscoll/Mr. S. Slosarik
P. O. Box 358
Sunnyvale, CA 94088

UNIVERSITIES

Department of Physics and Astronomy
Ball State University
ATTN: Mr. S. Mrozowski
Muncie, IN 47306

Franklin Institute Research Labs.
Physics of Materials Laboratory
Material and Physical Sciences Dept.
ATTN: Mr. J. Meakin, Manager
Benjamin Franklin Parkway
Philadelphia, PA 19103

Applied Physics Laboratory
The Johns Hopkins University
ATTN: Mr. W. Caywood
Johns Hopkins Road
Laurel, MD 20810

Department of Materials Science and
    Engineering
Massachusetts Institute of Technology
ATTN: Dr. D. Uhlmann
Boston, MA 02139

Massachusetts Institute of Technology
ATTN: Mr. J. May
        Dr. J. W. Mar
Boston, MA 02139

Aeronautical Research Associates of
    Princeton
ATTN: Dr. T. McDonough
Washington Road
Princeton, NJ 08540

Materials Science Department
Pennsylvania State University
ATTN: Dr. P. Walker
State College, PA 16801

Department of Materials Engineering
Rensselaer Polytechnic Institute
ATTN: Dr. J. Diefendorf
Troy, NY 12181

Southern Methodist University
Civil and Mechanical Engineering
    Department
ATTN: Dr. R. M. Jones
Dallas, TX 75275

University of California, Los Angeles
School of Engineering and Applied Science
ATTN: Dr. G. Sines
Los Angeles, CA 90024

Department of Mining, Metallurgical
    and Ceramic Engineering
University of Washington
ATTN: Mr. D. Fischbach
        Mr. D. Uptegrove
Seattle, WA 98195

University of Wyoming
Department of Mechanical Engineering
ATTN: Dr. D. Adams
Laramie, WY 82071

University of Southern California
ATTN: Mr. T. Yen
Los Angeles, CA 90007